UNIVERSITY OF OKLAHOMA

GRADUATE COLLEGE

STUDY OF CO_2 SOLUBILITY IN BRINE AND MINERALIZATION IN MAFIC BASALTIC FORMATIONS

A THESIS

SUBMITTED TO THE GRADUATE FACULTY

In partial fulfillment of the requirement for the

Degree of

MASTER OF SCIENCE

By

QAIS AL MAQBALI

Norman, Oklahoma

2023

STUDY OF CO_2 SOLUBILITY IN BRINE AND MINERALIZATION IN MAFIC BASALTIC FORMATIONS

A THESIS APPROVED FOR THE

MEWBOURNE SCHOOL OF PETROLEUM AND GEOLOGICAL ENGINEERING

BY THE COMMITTEE CONSISTING OF

Dr. Xingru Wu, Chair

Dr. Rouzbeh Ghanbarnezhad Moghanloo

Dr. Mashhad Fahes

Acknowledgments

Allhamdulliah, the work I have accomplished in this study would not have been possible without Allah (God) help. Thanks to Allah for giving me the patience, the guidance, and the knowledge to do this work.

I would like to thank Dr. Xingru Wu of the Mewbourne School of Petroleum and Geological Engineering tremendously for being the best advisor that I could have hoped for. Dr. Wu has provided me with the guidance and support that I needed to complete this work. I am thankful for Dr. Wu for his patience and sincerity in dealing with me throughout the research. The knowledge I gained from working with Dr. Wu is career changing one; there is always something new I learn from him in almost every single meeting we have.

I would also like to thank my thesis committee members, Dr. Rouzbeh Ghanbarnezhad Moghanloo and Dr. Mashhad Fahes from Mewbourne School of Petroleum and Geological Engineering for their insightful feedback on this research.

I would like to thank all my OU friends that made the collage experience much better and living away from home much easier.

Last but not least and most importantly, I would like to thank my parents for their unconditional support and for keeping me always in their prayers.

Table of Contents

Acknowledgments iv

Table of Contents v

List of Figures viii

List of Tables xiii

Abstract xiv

Chapter 1 - Introduction 1

1.1. Overview 1

1.2. Objective and Scope of Work 3

Chapter 2 - Literature Survey 5

2.1. Status of CO_2 Emission 5

2.2 Status of CO_2 Sequestration 9

2.3. CO_2 Geological Storage Methods 13

A. Depleted oil and gas Reservoirs 13

B. Deep Saline Aquifers 14

C. Coal Beds 16

D. Salt Caverns 17

E. Deep Oceans 19

2.4. Research Status and Key Observations on CO_2 mineralization 23

A. Overview 23

B. Case Studies and key Observations 25

Chapter 3 - Solubility of CO_2 in Brine 36

3.1. Overview 36

3.2. CO_2 solubility models and Key Findings 39

Chapter 4 - Modeling CO_2 mineralization in Mafic basaltic formation 47

4.1. Base Model 47

A. Static Model Description 47

B. Structural and Residual Trapping Modeling 48

C. Solubility Trapping Modeling 50

D. Mineral Trapping Modeling 51

4.2. Sensitivity Cases 55

Chapter 5 - Numerical simulation and discussion of CO_2 Mineralization in mafic basaltic formations 56

5.1. Base Model Results 56

5.2. Sensitivity Analysis 65

A. CO_2 mineralization effect on pressure and plume migration 66

B. Brine Salinity 68

C. Temperature 70

D. pH 71

Chapter 6 - Conclusions and future work 73

6.1. Conclusions 73

6.2. Future work 75

References 77

List of Figures

Figure 2-1. Global CO_2 emissions by fuel type (Ritchie et al. 2020). 5

Figure 2-2. Global CO_2 emissions by sector (Ritchie et al. 2020). 6

Figure 2-3. CO_2 emissions increase with urbanization as energy consumption increases as well (Dong et al. 2019). 6

Figure 2-4. Advance economics emissions are decreasing per year, unlike emerging economics (IEA 2022). 7

Figure 2-5. CO_2 emissions per capita (Ritchie et al. 2020). 8

Figure 2-6. Planned and implemented CCUS projects (Martin-Roberts et al. 2021). 9

Figure 2-7. Salt caverns are more geotechnically favorable in salt domes and thick-bedded salt (Warren 2017). 19

Figure 2-8. CO2 phases in the ocean at different depth (Adams and Caldeira 2008). 20

Figure 2-9. CO_2 density decreases below the seafloor due to the higher temperature(House et al. 2006). 22

Figure 2-10. CO_2 storage in the deep ocean sediments. CO2 hydrates act a seal to the liquid CO2 before dissolving in pore fluid (House et al. 2006). 22

Figure 2-11. CO_2 trapping mechanisms in a) sedimentary formations and b) basalt formations (Raza et al. 2022). 25

Figure 2-12. CO_2 mineralization decreases with decreasing the reactive surface area (RSA). D: the grain diameter that is used to calculate RSA (Luo et al. 2012). 27

Figure 2-13. The rate of mineralization is higher at lower pH values (Zhang and DePaolo 2017). 28

Figure 2-14- most of CO_2 mineralization occurs away from the fracture inlet. 30

Figure 2-15. Porosity alteration occurs around the wellbore due to the dry-out effect near the wellbore and due to CO2 mineralization in the other zones (André et al. 2007). 32
Figure 2-16- Mineral dissolution is CO_2 saturated water is lower at higher temperatures (Li et al. 2018). 34
Figure 3-1. CO_2 solubility as a function of pressure at constant temperature of 300 K and constant salinity of 1 mol/kg-H2O. All models show that CO_2 solubility increases with pressure. 43
Figure 3-2. CO_2 solubility as a function of pressure at constant temperature of 330 K and constant salinity of 1 mol/kg-H2O. All models show that CO_2 solubility increases with pressure. CO_2 solubility is lower at 330 K than 300 K. Thus, CO_2 solubility decreases with temperature. 43
Figure 3-3. CO_2 solubility as a function of pressure at constant temperature of 360 K and constant salinity of 1 mol/kg-H2O. All models show that CO_2 solubility increases with pressure. CO_2 solubility is lower at 360 K than 330 K. Thus, CO_2 solubility decreases with temperature. 44
Figure 3-4. CO_2 solubility as a function of salinity at constant temperature of 330 K and constant pressure of 2500 psi. All models show that CO_2 solubility decreases with salinity. 44
Figure 3-5. CO_2 solubility as a function of salinity at constant temperature of 330 K and constant pressure of 2500 psi. All models show that CO_2 solubility decreases with salinity. CO_2 solubility is lower at 360 K than 330 K. Thus, CO_2 solubility decreases with temperature. 45
Figure 3-6. CO_2 solubility as a function of salinity at constant temperature of 330 K and constant pressure of 2500 psi. All models show that CO_2 solubility decreases with salinity. CO_2 solubility is lower at 330 K than 300 K. Thus, CO_2 solubility decreases with temperature. 45
Figure 3-7. Estimated and experimental CO_2 solubility as function of pressure. The change in the slope indicated the phase change of CO2 to liquid (Sadeghi et al. 2015). 46

Figure 4-1. The reservoir model is designed with 15 layers with a total depth of 225 ft. The injection well is centered in the middle of the model and will inject 200 MCF/day for 4 years.. 47

Figure 4-2. Brine and CO2 relative permeability as a function of water saturation. Irreducible water saturation is 25% while critical gas saturation is 25%. 49

Figure 4-3. Rate Constant changes with depth due to the temperature increases. Higher temperature increases the rate constant and consequently the reaction rate. 53

Figure 5-1. Average reservoir pressure declines significantly after injection shut-in due to the continuous CO2 mineralization. 56

Figure 5-2. 95% of injected CO2 mineralized within the first 7 years. CO2 mineralization continues after 7 years but at very low rate. 57

Figure 5-3. The dissolution of forsterite and wollastonite are the source of magnesium and calcium to mineralize CO2 into calcite and magnesite. Enstatite has a negative effect of CO2 mineralization because its precipitation consumes magnesium ions. 58

Figure 5-4. CO2 mineralized into calcite (10%) and magnesite (90%). Magnesite continues to precipitate for 200 years due to the continuous dissolution of forsterite. 59

Figure 5-5. The amount of supercritical CO2 declined rapidly after injection shut-in due to dissolution in brine. The dissolution of CO2 in brine continuous for 200 years which results in releasing carbonate ions to bond with calcium and magnesium. 59

Figure 5-6. Maximum CO_2 saturation is 65.5% which is observed near wellbore at the end of injection. The plume migrated a maximum of 105 ft horizontally and 110 ft vertically from the upper perforation. 61

Figure 5-7. CO_2 plume migration after (A) 4 years, (B) 25 years, (C)100 years and (D) 200 years. CO_2 plume declines due to dissolution in brine. 61

Figure 5-8. The dissolution of CO_2 in brine releases hydrogen ions that lower the pH in the brine. This pH is increased as CO_2 mineralizes into carbonate minerals. Brine pH after (A) 4 years, (B) 25 years, (C)100 years and (D) 200 years..... 62
Figure 5-9. Porosity reduces due to the additional cement in the pore space due to CO_2 mineralization. porosity reduced by 5% near wellbore. Porosity changes after (A) 4 years, (B) 25 years, (C)100 years and (D) 200 years..... 64
Figure 5-10. The change in permeability is expressed as a resistance factor. The maximum resistance factor is obtained near wellbore which is 3.5 resulting in reducing the permeability from 100 md to 28.5 md. Resistance factor over time at after 4 years, (B) 25 years, (C)100 years and (D) 200 years..... 65
Figure 5-11. Average reservoir pressure is significantly lower when CO_2 mineralization is considered. 66
Figure 5-12. CO_2 plume reaches the top layer at the end of the simulation for Case 1 and 2 unlike Base Case where mineralization is simulated. Thus, stored CO_2 in basalt formations has a very low risk of leakage to the surface. A) CO_2 plume at the end of injection, B) CO_2 plume after 200 years. 67
Figure 5-13. CO_2 dissolution in brine is higher at lower salinities. 68
Figure 5-14. CO_2 mineralization at different brine salinity. There is a slight effect on the amount of CO_2 mineralized as salinity changes. 69
Figure 5-15. Magnesium concentration in brine stabilizes after 7 years at different salinities. ... 69
Figure 5-16. CO_2 mineralization at different temperatures. CO_2 is mineralized at higher volumes in lower temperatures..... 70
Figure 5-17. Forsterite dissolves faster in brine at higher temperatures. 71

Figure 5-18. CO_2 mineralizes at a faster rate in lower pH brine..... 72

Figure 5-19.Dissolved CO_2 in Case 10 declines throughout the 200 years which indicate a slow rate of mineralization. 72

List of Tables

Table 2-1- Operating CCUS projects around the world (IEA 2020). 12

Table 3-1. coefficients that are used to calculate a, b, and c in CO2 solubility model of 41

Table 4-1. Reservoir static model inputs. 48

Table 4-2. Chemical reactions inputs..... 54

Abstract

A huge amount of CO2 emissions should be mitigated for environmental benefits and to reach net zero by 2050. One method to mitigate these emissions is permanent CO_2 sequestration through mineralization. CO_2 can be mineralized as carbonate minerals such as calcite and magnesite if injected into igneous formations rich in reactive minerals such as olivine, pyroxene and plagioclase. The dissolution of CO_2 in brine is the first geochemical reaction in the pore space that leads to CO_2 mineralization eventually. The objective of this study is to understand the dynamics and controlling parameters of CO_2 dissolution in brine and mineralization in mafic basaltic formations.

This study uses a 3D carbon sequestration numerical model to simulate the geochemical reactions of injecting CO_2 into a saline aquifer in a basaltic formation. The model includes three main geochemical reactions: CO_2 dissolution in water, dissolution of formation minerals, and precipitation of carbonate minerals. The first reaction results in forming carbonic acid that reacts with the formation minerals: anorthite, wollastonite, pyroxene, and olivine, which results in releasing calcium and magnesium ions. The reaction between divalent cations and dissolved CO_2 in brine results in precipitating carbonate minerals: magnesite and calcite. CO_2 is injected into the formation for four years and simulated for 200 years. The dynamics of reservoir pressure and CO_2 plume migration are studied as CO_2 mineralizes. In addition, the rate of mineral dissolution and precipitation is analyzed as the initial conditions of the reservoir change, including brine salinity, temperature, and pH. In addition, the change in porosity and permeability is investigated during CO_2 mineralization process.

The results show that 95% of the injected CO_2 is mineralized within the first 7 years. After 200 years, 98% of injected CO_2 is mineralized, 1.5% is dissolved in brine and 0.5% is residually

trapped. Due to the mineralization of CO_2 in the form of magnesite, and calcite, the porosity decreased by 5% maximum due to the extra cement in the pore space. Likewise, permeability decreases by 71%. The reservoir pressure increases during the injection but reduces by 15% after 200 years due to continuous CO_2 mineralization. Lower reservoir temperature increases the amount of CO_2 mineralized due to the higher CO_2 solubility in water. Brine salinity has minimal effect on CO_2 mineralization. The rate of CO_2 mineralization is higher when the initial pH in a reservoir is lower.

The carbon storage numerical model built for this study considers the effect of the formation water chemistry and rocks mineralogy on the amount of CO_2 sequestrated. In addition, it shows the advantage of targeting basaltic formations for CO_2 storage compared to sedimentary formations. In addition, this study shows that CO_2 can be stored permanently in the subsurface with no risk of leakage.

Chapter 1 - Introduction

1.1. Overview

The current CO_2 emissions must be mitigated to decrease the risks of climate change and reach net zero by 2050. The amount of CO_2 emissions differs by fuel type and sector type. Fossil fuels are the main source of CO_2 emissions in terms of fuel type, while electricity and heat production are the main sources of CO_2 emissions by sector type (Ritchie et al. 2020). As the economy of a society grows, the energy demand grows with it, leading to more CO_2 emissions. Thus, CO_2 emission increases with urbanization (Dong et al. 2019). On the other hand, in advanced economies countries such as the United States and European Union counties emissions are declining per year due to the conversion from depending on fossil fuel as the primary source of energy toward renewable energy sources besides implementing new technologies to reduce CO_2 emissions from fossil fuels (IEA 2022). China, Russia and India are in the top 4 countries in CO_2 emissions due to their dependence on coal as the primary energy source (Ritchie et al. 2020).

Since 2009, CO_2 sequestration projects have been proposed to reduce CO_2 emissions; however, most of them were not implemented. At the current devilment rate of carbon capture, storage, and utilization (CCUS) projects, net zero emission by 2050 is impossible (Martin-Roberts et al. 2021). Thus, the rate of CCUS projects must be increased and governments should support this by providing financial incentives and guidance for the safe sequestration of CO_2 (IEA 2020).

Options to store CO_2 in the subsurface include depleted oil and gas reservoirs, deep saline aquifers, unmineable coal seams, salt caverns, and deep oceans. Each storage method has a different storage capacity and unique challenges. Deep oceans have the largest storage capacity, followed by deep saline aquifers and depleted oil and gas reservoirs. The main challenges of

implementing these technologies include cost, location selection, leakage risk and the availability of required infrastructure and technologies (Voormeij and Simandl 2002).

Carbon dioxide (CO_2) sequestration in deep saline aquifers has been proven to be a promising technique to mitigate CO_2 emissions for environmental benefits (Birkholzer et al. 2015, Kumar et al. 2005, Pruess and Garcia 2002). CO_2 can be stored in deep saline aquifers physically and chemically, which occurs together once CO_2 is injected into subsurface formations. Physical storage through sealed geological formation, residual gas trapping, and chemical storage through solubility trapping and mineralization. Physical trapping mechanisms have the risk of CO_2 leakage, while chemical trapping has a low risk, but it takes a very long time to occur in sedimentary and carbonate formations (Bachu 2008). Thus, in recent years, many studies have been accomplished to investigate CO_2 storage in deep saline aquifers of basaltic formations that combine the benefits of low leakage risk and quick chemical trapping(Raza et al. 2022, Xiong et al. 2018, Snæbjörnsdóttir et al. 2020).

Basalt formations have a high potential of storing CO_2 in the form of carbonate minerals. Basalt rocks consist of highly reactive minerals, including plagioclase, pyroxene, and olivine, and these minerals are rich in magnesium, calcium, and iron (Dabirian et al. 2012, Moita et al. 2020, Olajire 2013). The reaction of dissolved CO_2 and these minerals lead to CO_2 mineralization in the form of magnesite, calcite, and siderite (Daval et al. 2009, Hangx and Spiers 2009). Other minerals that can be found alongside mafic formations, such as wollastonite can contribute to more CO_2 mineralization due to its high content of calcium (Ding et al. 2014, Kashim et al. 2020). Wollastonite has the potential to be found alongside basaltic formation because it forms through magma crystallization or a high increase in the temperature of limestone and silica in deep formations (Ciullo and Robinson 2002).

The process of CO_2 carbonation in the subsurface goes through three phases: (1)- CO_2 dissolution in water, (2)- reservoir mineral dissolution, and (3)- carbonate mineral precipitation (Mitchell et al. 2010, Raza et al. 2022). In addition to mineral species and their compositions, the amount and reaction dynamics of CO_2 mineralized depend highly on the reservoir characteristics. A high porosity and permeability reservoir have a higher reactive surface area for CO_2 to react with minerals (Beckingham et al. 2016, Kieffer et al. 1999). In addition, CO_2 solubility in the water depends on the reservoir temperature, pressure, and water salinity. CO_2 dissolution in water has a positive correlation with pressure and a negative correlation with temperature and salinity (Steel et al. 2016, Luhmann et al. 2014).

1.2. Objective and Scope of Work

The objective of this research is to study the geochemical reactions of CO_2 in deep saline aquifers of basaltic formations through conducting a 3D numerical simulation. The study includes:

1. **CO_2 solubility in brine**
    A. Understanding the dynamics of CO_2 dissolution in the brine
    B. CO_2 solubility and chemical potential at equilibrium
    C. Understanding the importance of Henry's law of solubility.
    D. Comparing Duan and Sun (2003) model, Chang et al. (1996) model and Spycher et al. (2003) to estimate CO_2 solubility in water as a function of pressure, temperature, and salinity.
    E. Literature review of CO_2 solubility model and key findings.
2. **Building a 3D model to simulate CO_2 trapping in basaltic formations.**
    A. Identifying CO_2 trapping mechanism in the model.

B. Identifying governing equations to simulate CO_2 physical and chemical trapping.

C. Identifying basalt mineralogy and possible chemical reactions with CO_2

D. Designing sensitivity cases to study the effect of salinity, temperature and pH on the rate and quantity of CO_2 mineralization.

3. CO_2 **mineralization analysis**

A. The change in the reservoir pressure due to CO_2 injection and mineralization.

B. The dissolution of basalt minerals and precipitation of carbonate minerals.

C. The change in porosity and permeability due to CO_2 mineralization.

D. The change in brine pH due to CO_2 dissolution.

E. Sensitivity analysis of salinity, temperature, pH, reactive surface area and activation energy on CO_2 mineralization.

Chapter 2 - Literature Survey

2.1. Status of CO_2 Emission

To reach net zero by 2050, the current CO_2 emissions must be mitigated. The world produced around 36.3 $GtCO_2$ in 2021 which is 6% higher than that of 2020. The CO_2 emissions in 2020 plumed by 5.1% from 2019 due to the COVID-19 pandemic as human activities, transportation, and overall energy demand declined due to the policies adopted to mitigate the risk of the pandemic spread (IEA 2022). Most of the CO_2 emissions come mainly from fossil fuels as shown in Figure 2-1. The leading sector in greenhouse emissions is electricity and heat production, transportation, manufacturing and construction, and agriculture. As shown in Figure 2-2, electricity and heat count for 24.2% of the total greenhouse emissions, and transportation counts for 16.2% (Ritchie et al. 2020).

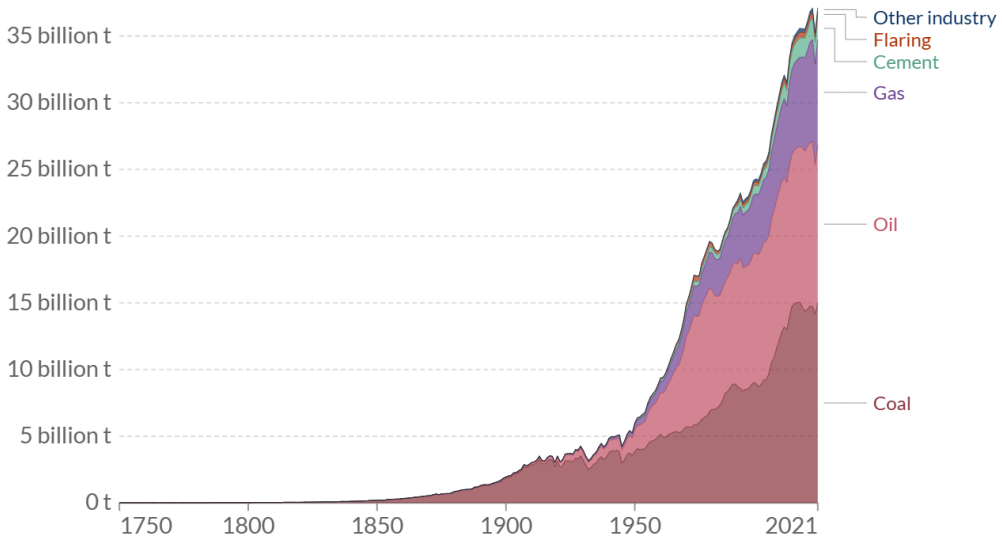

Figure 2-1. Global CO_2 emissions by fuel type (Ritchie et al. 2020).

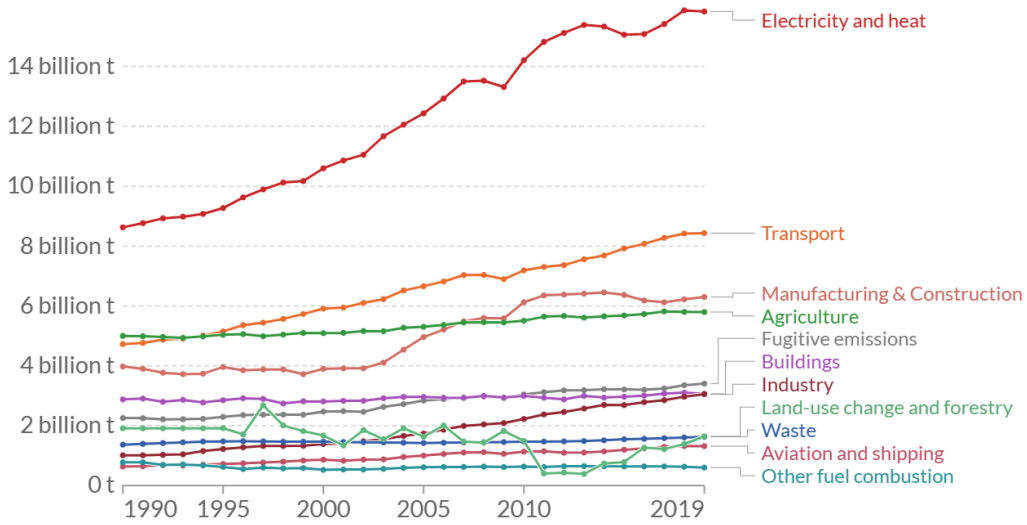

Figure 2-2. Global CO_2 emissions by sector (Ritchie et al. 2020).

Most of the CO_2 emissions are produced in the developed countries that have the highest quality of life. As the economy of a country grows, the amount of CO_2 emissions increases due to the higher demand for energy that is required for industrialization and urbanization. On the other hand, countries with the strongest economies can shift toward more renewable energy usage due to their financial capabilities compared to countries with weaker economies. Figure 2-3 shows the relationship between the amount of CO_2 emissions and communities' urbanization (Dong et al. 2019).

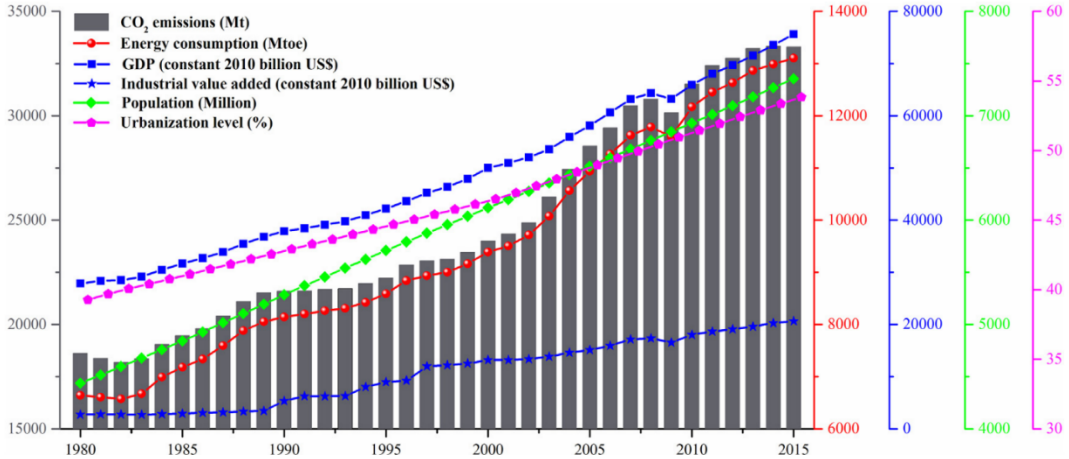

Figure 2-3. CO_2 emissions increase with urbanization as energy consumption increases as well (Dong et al. 2019).

CO_2 emissions from countries with strong economies such as the United States, European Union, and Japan are declining yearly. On the other hand, the CO_2 emissions from emerging economies countries experiencing accelerated growth in their economies, such as China and India are increasing per year as shown in Figure 2-4 (IEA 2022).

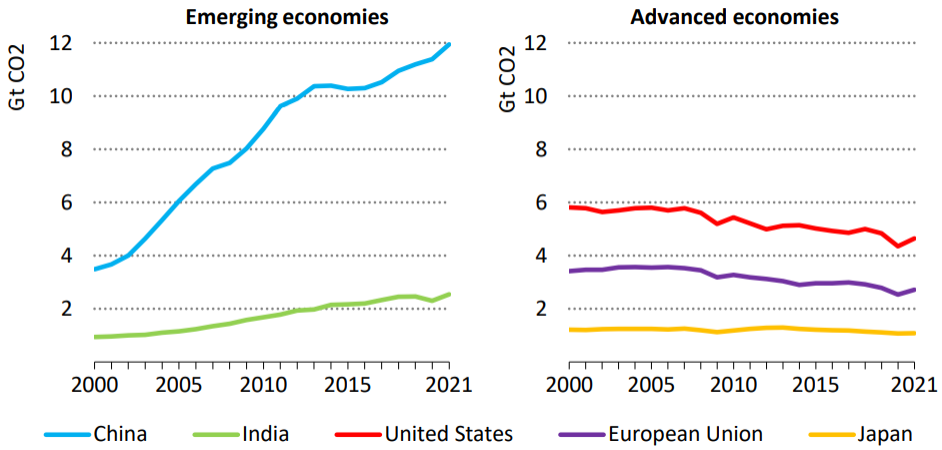

Figure 2-4. Advance economics emissions are decreasing per year, unlike emerging economics (IEA 2022).

China is the leading country in total greenhouse emissions due to its dependence on coal for energy production. In 2021, China produced 11.47 billion tonnes of greenhouse emissions, around 30% of total global emissions. In China, coal counts for 70% of greenhouse emissions. The United States comes second in the total global greenhouse emissions, followed by India and Russia. In 2021, the United States produced 5.01 billion tonnes of greenhouse emissions; oil, gas and coal accounted for 44%, 32.7%, and 20%, respectively. India is similar to China, where it depends on coal as the main energy source. In 2021, coal contributed to 66.4% of India's total greenhouse emissions of 2.71 billion tonnes. Russia's emissions mainly come from gas usage, contributing to around 50% of total Russia's greenhouse emissions in 2021 (Ritchie et al. 2020). The total CO_2 emissions in a country are affected directly by the population. Thus, it is no wonder that China is leading the world in its contribution to the total global emissions of CO_2.

The highest CO_2 emissions per capita come from counties with high oil and gas production and low populations. The leading countries in CO_2 emissions per capita are Qatar, Trinidad and Tobago and Kuwait, with estimated emissions of 49 tonnes, 30 tonnes, and 25 tonnes per capita, respectively. As shown in Figure 2-5, Canada and the United States are leading the developed countries in CO_2 emissions per capita, followed by China and South Africa (Ritchie et al. 2020). Due to the increase in the use of renewable energy sources and adapting policies to mitigate CO_2 emissions, since the beginning of the 2000s, CO_2 emissions per capita have been declining in the United States, Canada, and European Union. On the other hand, the emissions per capita in China and India are continuously increasing due to the continuing and increasing dependence on

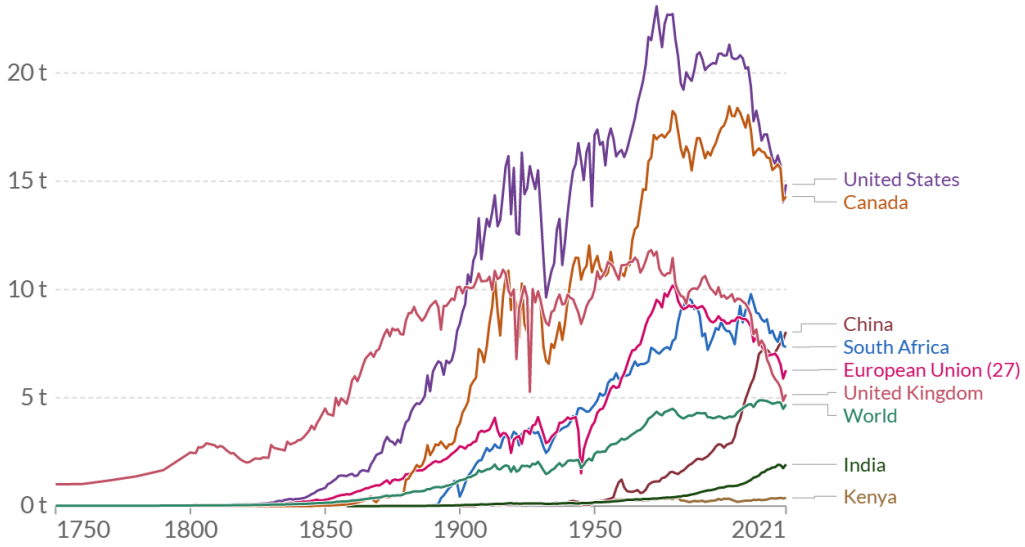

Figure 2-5. CO_2 emissions per capita (Ritchie et al. 2020).

coal as the main energy production source.

To reach net zero by 2050, CO_2 emissions must be reduced significantly through the shift toward the usage of renewable energy, improving the current oil and gas facilities to limit greenhouse leakage and CO_2 sequestration and utilization. The next part of this chapter will discuss CO_2 sequestration and utilization options.

2.2 Status of CO_2 Sequestration

CO_2 emissions can be reduced by implementing large-scale CO_2 capture and storage (CCS) projects. CCS will play a critical role in achieving a net zero by 2050. However, the development of CCS projects in the last decade has been slow and does not meet global expectations. The movement toward implementing large-scale CCS projects started in 2008 with the G8's agreement to implement CCS projects to mitigate CO_2 emissions. The current rate of CCS project development must be increased significantly to reach global goals by 2050. If the current development rate stays the same, only 10% of the target emissions will be stored by 2050 (Martin-Roberts et al. 2021).

Much research has been done to demonstrate the success of CCS projects; however, financial risk, governmental policies and market instability are the main reasons for the slow progress of

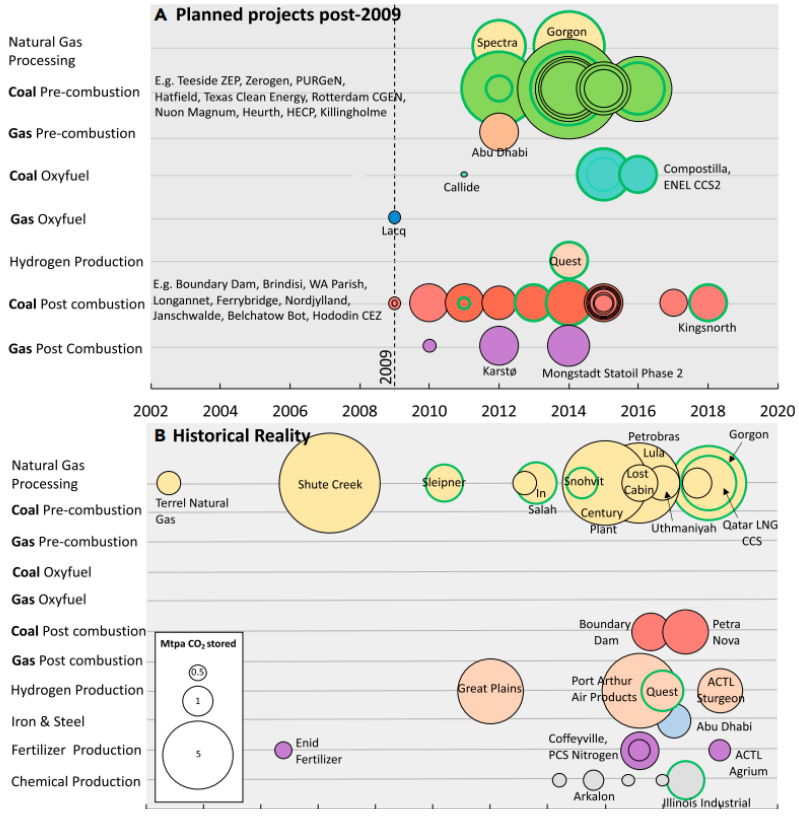

Figure 2-6. Planned and implemented CCUS projects (Martin-Roberts et al. 2021).

CCS projects. Numerous projects have been planned between 2009 and 2021 to equip coal power plants with CCS facilities since coal power plants are a major producer of CO_2 emissions. A total of 42 projects have been planned, but only 20 have been successfully implanted. Figure 2-6 shows the number of CCS projects planned to be implemented after 2009 and compared to successfully implanted projects (Martin-Roberts et al. 2021).

Only six projects worldwide are dedicated to capturing and storing CO_2 permanently in the subsurface: the Illinois industrial, Snøhvit and Sleipner in Norway, Quest in Canada, Gorgon in Australia, and Qatar's LNG plant (Martin-Roberts et al. 2021). These six projects store 7 million tonnes of CO_2 per year. The term CCS is changed to CCUS, which stands for carbon capture, utilization, and storage, to include projects where CO_2 is used to produce or enhance the production of a new product. There are 15 CCS operating projects where the captured CO_2 is used for enhanced oil recovery (EOR) (IEA 2020). Storing CO_2 through EOR projects is less effective than permanent geological storage. Most of the CO_2 used in EOR projects is not sourced from power plants but is produced as a side product from oil and natural gas production and then reinjected back into the subsurface (Voormeij and Simandl 2002). Table 1 shows the current operating projects dedicated to CO_2 geological storage or EOR.

The Covid-19 pandemic further slowed the implementation of CCUS projects; however, as the economy recovers post-pandemic, more projects have been planned to be implemented. To encourage more investment in CCUS projects, global governments have started to change their policies. Governmental policies play a crucial part in CCUS projects. The first dedicated project for CO_2 storage is Slepiner which has been operating since 1996. In 19961, the Norwegian government imposed a tax on CO_2 emissions from offshore oil and gas projects, which encouraged the implementation of the Slepiner project due to the financial advantages. The

United States has adopted new tax policies called 45Q tax credits, which grant tax incentives for storing CO_2. The United States started storing CO_2 in subsurface formation earlier than Norway with the Val Verde project in Texas in the early 1970s. However, this project was not dedicated to storing CO_2 but rather using CO_2 to enhance oil recovery (IEA 2020).

There is a vast geological storage capacity for CO_2 worldwide. The United States is the leading country in the available CO_2 storage capacity with 800 gigatons. The US has the advantage of proximity between the target formations for CCUS projects and CO_2 point sources. In addition, the US has the largest pipeline network that extends approximately 5000 miles across the country which can be used to deliver captured CO_2 and point sources to storage sites. Europe's storage sites are mainly located in the North Sea, which is in proximity to many European countries. The United Kingdom has the largest storage capacity in Europe with 78 gigatons, followed by Norway with 56 gigatons and Germany with 20 gigatones. The total storage capacity in Europe is estimated to be around 300 gigatons. China has an estimated storage capacity of 425 gigatons (IEA 2020).

Table 2-1- Operating CCUS projects around the world (IEA 2020).

Country	Project	Operation date	Source of CO_2	CO_2 capture capacity (Mt/year)	Primary storage type
United States (US)	Terrell natural gas plants (formerly Val Verde)	1972	Natural gas processing	0.5	EOR
US	Enid fertiliser	1982	Fertiliser production	0.7	EOR
US	Shute Creek gas processing facility	1986	Natural gas processing	7.0	EOR
Norway	Sleipner CO_2 storage project	1996	Natural gas processing	1.0	Dedicated
US/Canada	Great Plains Synfuels (Weyburn/Midale)	2000	Synthetic natural gas	3.0	EOR
Norway	Snohvit CO_2 storage project	2008	Natural gas processing	0.7	Dedicated
US	Century plant	2010	Natural gas processing	8.4	EOR
US	Air Products steam methane reformer	2013	Hydrogen production	1.0	EOR
US	Lost Cabin Gas Plant	2013	Natural gas processing	0.9	EOR
US	Coffeyville Gasification	2013	Fertiliser production	1.0	EOR
Brazil	Petrobras Santos Basin pre-salt oilfield CCS	2013	Natural gas processing	3.0	EOR
Canada	Boundary Dam CCS	2014	Power generation (coal)	1.0	EOR
Saudi Arabia	Uthmaniyah CO_2-EOR demonstration	2015	Natural gas processing	0.8	EOR
Canada	Quest	2015	Hydrogen production	1.0	Dedicated
United Arab Emirates	Abu Dhabi CCS	2016	Iron and steel production	0.8	EOR
US	Petra Nova	2017	Power generation (coal)	1.4	EOR
US	Illinois Industrial	2017	Ethanol production	1.0	Dedicated
China	Jilin oilfield CO_2-EOR	2018	Natural gas processing	0.6	EOR
Australia	Gorgon Carbon Dioxide Injection	2019	Natural gas processing	3.4-4.0	Dedicated
Canada	Alberta Carbon Trunk Line (ACTL) with Agrium CO_2 stream	2020	Fertiliser production	0.3-0.6	EOR
Canada	ACTL with North West Sturgeon Refinery CO_2 stream	2020	Hydrogen production	1.2-1.4	EOR

2.3. CO_2 Geological Storage Methods

As discussed in the previous section, there is a vast geological storage capacity around the world to store CO_2. The challenge is to find feasible solutions to take advantage of this storage capacity. There are different methods to store CO_2 in the subsurface, each with advantages and disadvantages. CO_2 geological storage techniques are as follows:

A. Depleted oil and gas Reservoirs

Depleted oil and gas reservoirs can be used to store CO_2. Storing CO_2 in Depleted oil and gas reservoirs has the advantage of knowing the reservoir properties. These reservoirs have been evaluated and well-studied to maximize oil and gas production. In addition, the risk of leaking CO_2 in these reservoirs is minimum since they have been trapping oil and gas for thousands of years, meaning they have proven seal rocks. Likewise, the infrastructure around depleted oil and gas reservoirs is well-developed. It can be repurposed for CO_2 transportation and injection, which provides a financial advantage and reduce the time to develop a CCS project (Agartan et al. 2018, Le Gallo et al. 2002, Hannis et al. 2017).

Some disadvantages are associated with using depleted oil and gas reservoirs for CCS projects. Injecting CO_2 into a formation as a supercritical fluid has a better storage efficiency than gas or liquid CO_2. In depleted oil and gas reservoirs, the reservoir pressure is low, causing a CO_2 phase change from supercritical fluid to gas. This phase change causes flow assurance issues around the wellbore (Hoteit et al. 2019). The phase change supercritical to gas can cause the formation of gas hydrates around the wellbore, causing injectivity issues. The formation of hydrates can lower the injectivity of CO_2 and the cooling effect might trigger some fracturing due to thermal stress (Mathias et al. 2010, Oldenburg 2007, Ziabakhsh-Ganji and Kooi 2014). In addition, the increase in CO_2 velocity due to the phase change can lead to erosion in the flow pipes. Also, the

bottom hole pressure and tubing head pressure might be impacted due to the backpressure formed as injected fluid density changes significantly (Hoteit et al. 2019). To reduce the hydrated formation effect, Hughes (2009) suggested using a control device to control the flow of CO_2 at the bottom of the injection pipe and the CO_2 expansion.

B. Deep Saline Aquifers

Deep saline aquifers have a very large storage capacity that can be used to store CO_2. All current CO_2 emissions until 2050 can be stored in deep saline aquifers without another storage option (Voormeij and Simandl 2002). However, like any other storage option, storing CO_2 in deep saline aquifers has advantages and disadvantages. Unlike depleted oil and gas reservoirs, deep saline aquifers require extensive studying and evaluation before implementing a CCS project.

A deep saline aquifer must be at least 2625 ft to keep the injected CO_2 as a supercritical fluid and prevent the formation of hydrates (Foroozesh et al. 2018, Jayasekara et al. 2020). A deep saline aquifer must have a cap rock to prevent the vertical migration of CO_2 to groundwater zones. Due to the density difference between brine and supercritical CO_2, CO_2 will migrate upward of shallow groundwater zones if not structurally trapped by an impermeable seal rock (White et al. 2003). In addition, CO_2 in saline aquifers can be trapped through residual, solubility and mineral trapping. Residual trapping due to the effect of the capillary pressure in small pore spaces where some CO_2 particles are separated from the plume and then encapsulated by brine. Solubility trapping occurs due to the dissolution of CO_2 in brine which lowers the pH of brine due to the interaction between hydrogen ions with matrix minerals. The dissolution of matrix minerals will produce cations that will react with carbonate ions produced from CO_2 dissolution, eventually leading to mineral trapping (De Silva et al. 2015, Celia et al. 2015). Even though mineral

trapping is the safest method to store CO_2 in saline aquifers, porosity and permeability are reduced due to the cement precipitation in pore space. As a result, pressure builds up in the reservoir leading to reducing CO_2 injectivity (Yang et al. 2010).

Site section is one of the challenges for implementing CCS in a deep saline aquifer. Besides having an impermeable cap rock, the aquifer must not have faults or fractures that might enhance the vertical migration of CO_2 to the subsurface. Also, the injection of CO_2 increases pressure in the reservoir, which might trigger the reactivation of faults and fracture in the reservoir, causing a micro seismic event (Sminchak et al. 2001). In addition, the areal extent and thickness of the aquifers are very important. A small aquifer will experience a quicker and higher change in pressure due to the closed boundary effect. The amount of CO_2 stored in a closed system boundary will is limited by the change in formation compressibility and water compressibility as reservoir pressures increase during CO_2 injection. The quick increase in pressure can be solved by introducing water production wells in the system to withdraw brine from the aquifer to provide more storage pore space for CO_2. In an open boundary system where the aquifer has a huge areal extent, and the pressure propagation through the reservoir does not reach the boundary quickly, the increase in reservoir pressure is slower and smaller than in a closed boundary aquifer and mainly limited near wellbore (Gorecki et al. 2009).

CCS in deep saline aquifers requires a huge development cost compared to depleted oil gas reservoirs. The huge cost comes from the tremendous amount of data collection required to evaluate and ensure the safety of the aquifer for CO_2 storage. Also, facilities and infrastructures must be developed to deliver and inject CO_2 into the subsurface (Yang et al. 2010).

C. Coal Beds

Coal Beds have a small CO_2 storage capacity compared to saline aquifers and depleted oil and gas reservoirs. Coal beds are estimated to have a storage capacity of more than 15 gigatons of CO_2 (Voormeij and Simandl 2002). Even though the storage capacity in unamiable coal beds is very small compared to other methods, it is still attractive due to its economic advantages. Enhanced coal bed methane (ECBM) is a similar mechanism to EOR, where CO_2 is injected into the formation to produce more hydrocarbons. CO_2 is trapped in coal seams through sorption, stratigraphic and structural trapping and solubility trapping (Ibrahim and Nasr-El-Din 2015, Corum et al. 2013). Sorption trapping involves two processes: adsorption and absorption. Sorption is the main trapping mechanism in coal seams. Coal seams have a unique structure of a coal matrix and natural fractures divided into face cleats and butt cleats (Shi and Durucan 2005b).

Injecting CO_2 into a coal seam causes a reduction in the partial pressure of methane. The lower partial pressure methane will follow from the coal matrix to the cleat network toward the wellbore, where it gets produced. The injected CO_2 will flow from the wellbore to the cleat network and eventually to the coal matrix (Godec et al. 2014). CO_2 and methane flow in the cleat network is governed by Darcy's law. In contrast, the flow in the matrix is governed by three gas diffusion mechanisms: surface diffusion, molecular diffusion, and Knudsen diffusion. Understanding CO_2 flow inside the pore structure is important because most of the injected CO_2 in coal seams is stored in the matrix rather than the cleat network (Shi and Durucan 2005b, White et al. 2005). Coal could be gas-wet or water-wet. It is better to inject CO_2 into gas-wet coal seams (are you sure it is gas-wet?) because CO_2 will diffuse at a higher rate from the cleat network to the matrix than a water-wet coal seam (Ibrahim and Nasr-El-Din 2015). The amount

of CO_2 stored due to adsorption depends on the adsorption affinity of CO_2 to coal. CO_2 has a higher affinity to coal than methane. Thus, upon the injection of CO_2 into coal seams, CO_2 will cause methane desorption from coal. CO_2 stored in coal seams during ECBM ranges between 2 to 10 times higher than methane produced (Shi and Durucan 2005b). Likewise, supercritical CO_2 has more affinity to coal than gas CO_2; thus, injecting CO_2 as a supercritical fluid will increase the amount of CO_2 stored (Mukherjee and Misra 2018). In addition, Ridha et al. (2017) also showed that using horizontal wells increases the amount of methane produced and CO_2 sequestered up to 3 times more than vertical wells.

As with any other sequestration method, storing CO_2 in coal beds has many challenges. Coal seams targeted for CO_2 storage must be unmineable where coal seams are not disturbed. The definition of unmineable coal seams changes over time as technology evolves, making it difficult to determine what is an unmineable coal seam. In addition, a limited amount of data is available to study and determine the best conditions to store CO_2 in coal seams. (Godec et al. 2014, Corum et al. 2013). Also, CO_2 sorption causes coal swelling, while methane desorption causes coal shrinkage. However, the swelling rate is higher than the shrinkage rate, leading to decreased cleat permeability and pressure build-up, reducing CO_2 injectivity (Su et al. 2019, Mukherjee and Misra 2018).

D. Salt Caverns

Salt caverns are man-made storage complexes where water is injected into salt deposits to dissolve salt and cavities for storage. Salt caverns have been used to store natural gas and fluid wastes, and recently, they have been targeted for carbon and hydrogen storage (Zhang et al. 2022). The storage capacity of salt caverns depends on the amount of dissolved salt during water injection. Salt caverns have a bigger storage capacity than other storage methods when compared

based on CO_2 stored per unit volume of the storage complex. In addition, other storage methods take a long time to reach their maximum storage capacity due to the slow processes of CO_2 solubility and mineralization that are observed after hundreds and thousands of years. CO_2 storage capacity in salt caverns ranges between 600 kg to 900 kg per unit volume of a cubic meter. This storage capacity can be reached quickly if a sufficient injection system is available on site (Bachu and Dusseault 2005).

Salt caverns have very good geological and chemical properties to store gas permanently (Zivar et al. 2021). Salt has very low permeability, which provides a strong seal against CO_2 leakage to shallower zones. In addition, salt has self-healing abilities where if fractures are caused during the injection or drilling operation, salt creep behavior will seal these fractures. The creep behavior in salt deposits occurs as the pressure inside the salt caverns changes. Before injecting CO_2 into salt caverns, the brine produced from water injection into salt deposits is extracted, reducing the pressure inside the caverns. Pressure reduction leads to salt deformation due to the overburden stress leading to cavern closure. Injecting CO_2 into salt caverns will lead to an increase in the internal pressure. However, CO_2 is more compressible than brine; thus, the creep behavior will not stop but slow down (Dusseault et al. 2004, Zhang et al. 2022).

The challenge of using salt caverns as a storage complex for CO_2 is their limited overall capacity compared to other methods (Shi and Durucan 2005a). However, salt caverns can store limited CO_2 until other methods are fully developed. In addition, cavern pressure must be carefully monitored during brine extraction and CO_2 injection to avoid any fracturing or cavern failure. Pressure build-up will continue slowly as creep behavior continues even after injecting CO_2(Bachu and Dusseault 2005). Salt caverns for CO_2 storage must be carefully selected. The best salt caverns for CO_2 storage are located at depths of 1000-1200 m (Zhang et al. 2022). In

addition, salt deposits must be very soluble, thick and continuous and not separated by non-salt layers or faults that might be leakage path for CO_2 as shown in Figure 2-7 (Warren 2017, da Costa et al. 2019).

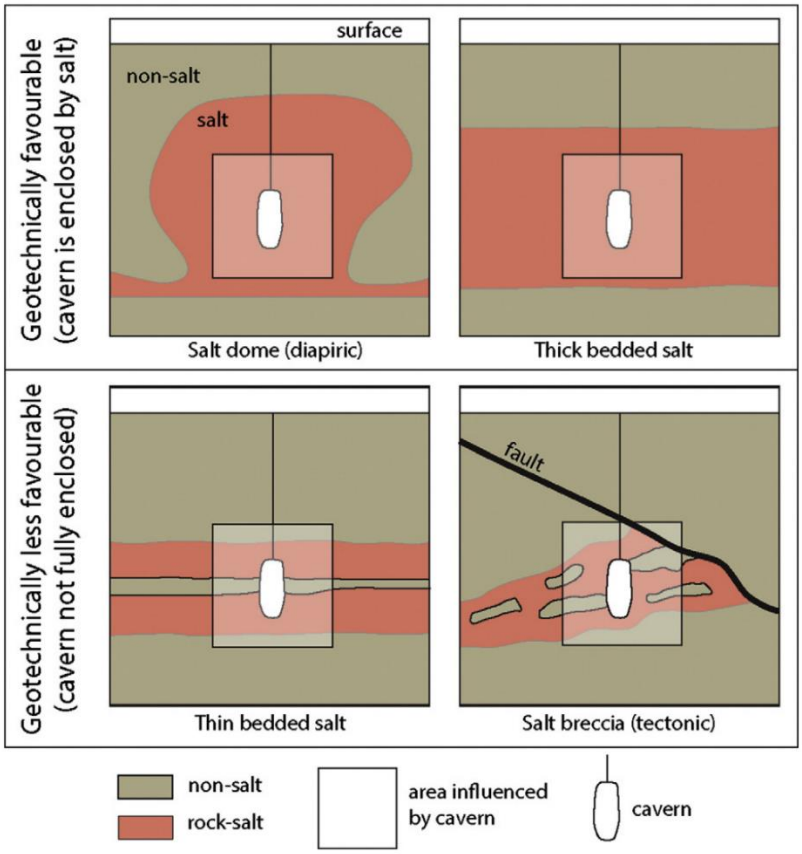

Figure 2-7. Salt caverns are more geotechnically favorable in salt domes and thick-bedded salt (Warren 2017).

E. Deep Oceans

Oceans naturally sink around seven gigatons of CO_2 annually (Caldeira et al. 2005). Oceans have the highest storage capacity of CO_2 when compared to other methods mentioned above (Voormeij and Simandl 2002). However, the real capacity of ocean storage of CO_2 depends on the ocean tolerance for chemical changes as CO_2 dissolves in a sweater without endangering the ocean ecosystem. Oceans can store up to 1000 gigatons of CO_2 if the pH change tolerance is 0.1.

In contrast, if the tolerance for pH change is 0.3, oceans can store up to 5600 gigatons of CO_2 (Adams and Caldeira 2008).

The phase of CO_2 stored in the ocean depends on depth, pressure, and temperature, as shown in Figure 2-8. CO_2 can be stored as gas, liquid, or hydrate. These different phases of CO_2 will dissolve in seawater resulting in solubility trapping and, consequently, mineral trapping due to the chemical reactions with carbonate sediments on the seafloor. CO_2 is delivered and injected into oceans at different depths, which will determine the initial phase of CO_2. If the injection depth is below 500 m (1640.4 ft), CO_2 will be in the gas phase, and below that will be in the liquid phase. Gas and liquid CO_2 have a lower density than seawater; thus, it will migrate upward due to gravity segregation forming a rising plume.

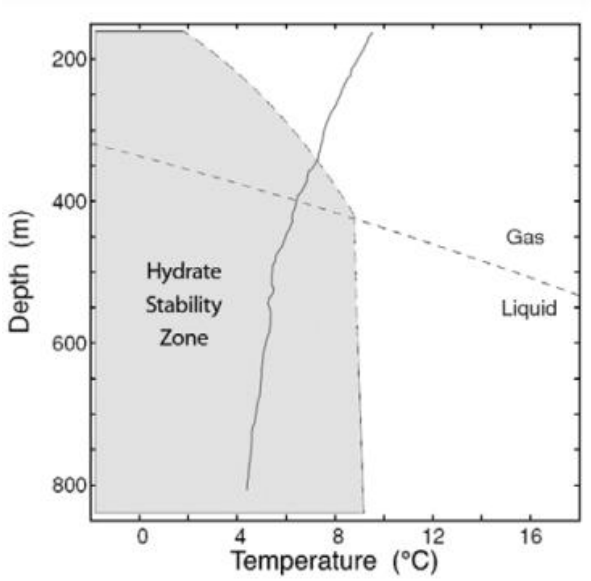

Figure 2-8. CO2 phases in the ocean at different depth (Adams and Caldeira 2008).

The injection method can promote the dissolution of CO_2 in seawater. Injecting CO_2 through ships is better than a fixed pipe system because the movement of the ship provides an additional dispersion of CO_2 in the ocean, which leads to more dissolution. In depths below 3000 m (9843 ft), the liquid phase of CO_2 will be denser than the seawater, causing it to sink to the seafloor,

forming a CO_2 lake. Also, CO_2 lakes at the bottom of the ocean can be created by injecting CO_2 directly into the bottom. In addition, at a depth below 400 m (1312 ft), CO_2 hydrates can form due to the high pressure and low temperature. Hydrates are crystalline cages of water molecules trapping CO_2 molecules inside them. Hydrates have a higher density than seawater; thus, they will sink to the bottom of the ocean due to gravity segregation. CO_2 hydrates are unstable and can dissolve in seawater but at a slower rate than liquid CO_2(Adams and Caldeira 2008, Caldeira et al. 2005). CO_2 lakes can be disrupted by ocean dynamics and currents, which can leak a huge amount of CO_2 on the surface (Sheps et al. 2009, House et al. 2006).

House et al. (2006) suggested the storage of CO_2 in the sediments below the seafloor. The geothermal gradient of the sediments below the seafloor is different from the ocean gradient. At a depth below 200 m (656 ft) below the seafloor, the liquid CO_2 will have a lower density and become buoyant due to the higher temperature. Two zones of pressure and temperature exist below the seafloor: the negative buoyancy zone (NBZ) and the hydrate formation zone (HFZ). NBZ is the first 200 m below the seafloor, where CO_2 still has a higher density than pore fluid, as shown in Figure 2-9. HFZ is the zone below the seafloor where temperature and pressure are adequate to form hydrates. Injecting liquid CO_2 below HFZ can lead to permanent CO_2 storage. As shown in Figure 2-10, hydrates in the HFZ act as a seal to the buoyant liquid CO_2 in the deep sediments of the seafloor. Over time, the hydrate cap will grow laterally, trapping CO_2 below it. At the same time, some CO_2 dissolves in the pore fluid, increasing the density of the pore fluid and resulting in downward migration into the deep sediments. Eventually, liquid CO_2 and hydrates will dissolve in the water inside the pore space. The resulting solution will be neutrally

buoyant due to the dissolution inside large volume of water over long period of time (House et al. 2006).

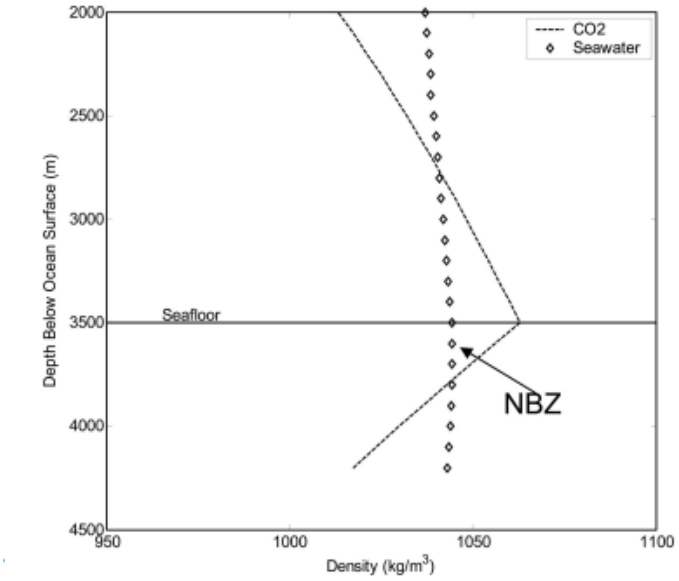

Figure 2-9. CO_2 density decreases below the seafloor due to the higher temperature(House et al. 2006).

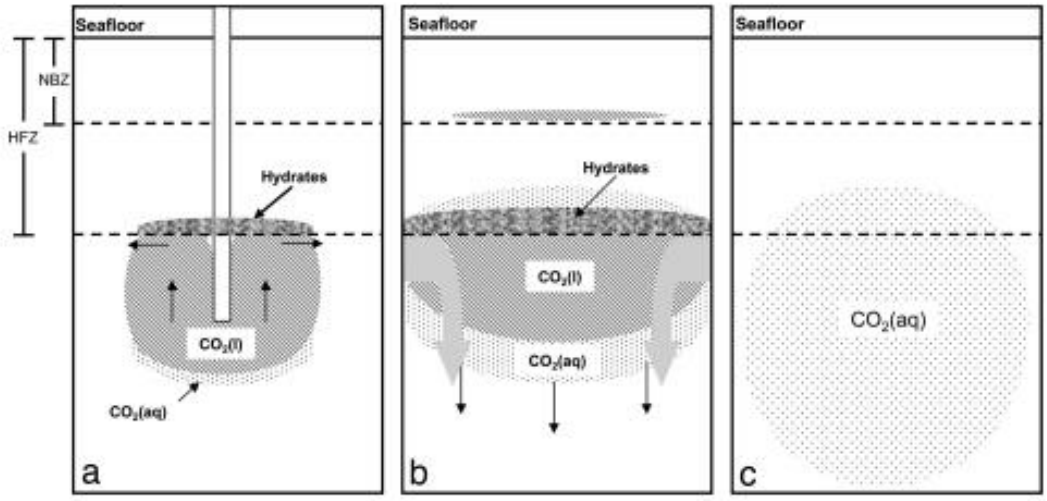

Figure 2-10. CO_2 storage in the deep ocean sediments. CO2 hydrates act a seal to the liquid CO2 before dissolving in pore fluid (House et al. 2006).

There are many environmental concerns regarding storing CO_2 in the oceans. The dissolution of CO_2 in seawater decreases the pH of seawater. The change in the chemical properties of seawater can lead to changing the ecological and physiological processes of some organisms in the oceans, such as calcification, growth, reproduction, and photosynthesis (Caldeira et al. 2005).

2.4. Research Status and Key Observations on CO_2 mineralization

A. Overview

CO_2 mineralization turns CO_2 into a solid deposit in the form of carbonate minerals. CO_2 mineralization occurs due to the interaction between the dissolved CO_2 in the brine and the formation of reactive minerals. Mineralizing CO_2 into carbonate minerals is the safest way of storing CO_2 in the subsurface because once CO_2 is mineralized, there is no risk of CO_2 upward migration that might lead to leakage. Many parameters control the mineralization process, including pressure, temperature, brine salinity, pH, existing reactive minerals in the formation, porosity, permeability, reactive surface area, and reaction activation energy. The process of in-situ CO_2 mineralization can be divided into three main reactions: 1) CO_2 dissolution in brine to produce hydrogen and carbonate ions, 2) formation minerals reaction with hydrogen to produce cations, and 3) carbonate ions and cations reaction to produce carbonate minerals (Romanov et al. 2015). The first chemical reaction of CO_2 dissolution in water is expressed as follows:

$$CO_2 + H_2O \leftrightarrow H^+ + HCO_3^-$$

$$CO_3^{2-} + H^+ \leftrightarrow HCO_3^-$$

$$H_2O \leftrightarrow H^+ + OH^-$$

The formation minerals' reactions with hydrogen produced from the above reaction depends on the rock type and what kind of reactive minerals it hosts. The reactive minerals in a sandstone

formation differ from those in a carbonate or igneous rock formation. The main products of the second reaction are mostly divalent cations such as calcium (Ca^{2+}), magnesium (Mg^{2+}), and iron (Fe^{2+}) (Romanov et al. 2015). These divalent cations react with bicarbonate to form calcium carbonate, magnesium carbonate, and iron (II) carbonate as follows:

$$HCO_3^- + Ca^{2+} \leftrightarrow CaCO_3 + H^+$$

$$HCO_3^- + Mg^{2+} \leftrightarrow MgCO_3 + H^+$$

$$HCO_3^- + Fe^{2+} \leftrightarrow FeCO_3 + H^+$$

There are other minerals that can be precipitated due to CO_2 injection such as dawsonite ($NaAlCO_3(OH)_2$) in sandstone formations (Romanov et al. 2015). Reservoir chemical equilibrium changes upon the injection of CO_2 because CO_2 dissolution in brine leads to lower pH of the pore fluids. This change triggers the series of mineral dissolution and precipitation to reach a new chemical equilibrium (Raza et al. 2022). CO_2 solubility in water is controlled by three main parameters that will be discussed in further detail in the next chapter.

The CO_2 mineralization rate in sedimentary formations is much lower than in volcanic or igneous formations. Sandstone is adequate targets to store CO_2 due to its high porosity and permeability, providing high storage capacity for CO_2. Also, Sandstone formations are sealed with low porosity and low permeability shale rocks that trap buoyant CO_2 from migrating to the surface. However, sandstone rocks are dominated by quartz with a small fraction of feldspar that is not very reactive with dissolved CO_2 to precipitate into carbonate minerals. Thus, a very low percentage of injected CO_2 is mineralized in sandstone formations even after thousands of years. On the other hand, volcanic or igneous formations are rich in minerals that have high reactivity with CO_2 and contain alkali cations that combine with carbonate ions to form carbonate minerals

(Snæbjörnsdóttir et al. 2020, Romanov et al. 2015). Figure 2-11 shows the difference in the trapping mechanism in sedimentary formations as compared to basalt formations. In basalt (volcanic rock), the trapping mechanics are solubility trapping and mineral trapping due to the high and quick reactivity between dissolved CO_2 and basalt minerals.

Basalt is the most attractive rock type in volcanic formations. Igneous rocks are subdivided into four categories based on mineral composition: felsic, intermediate, mafic and ultramafic. Mafic

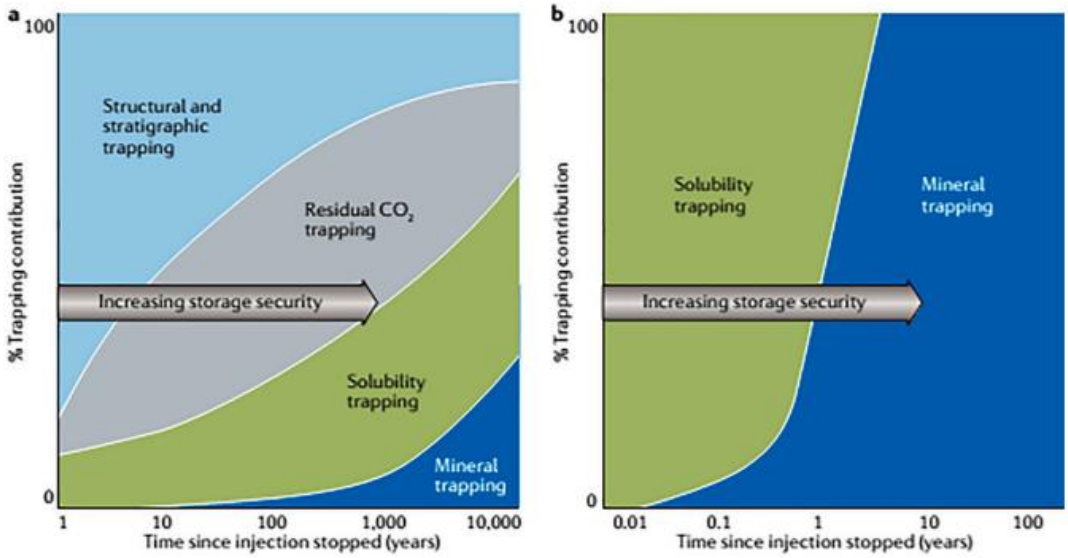

Figure 2-11. CO_2 trapping mechanisms in a) sedimentary formations and b) basalt formations (Raza et al. 2022).

and ultramafic rocks are targeted for CO_2 mineralization due to their mineral composition of reactive minerals such as olivine, pyroxene and plagioclase feldspar. Basalt comes under the mafic category (Raza et al. 2022).

B. Case Studies and key Observations

Over the last decade, there has been a tremendous interest in investigating the reservoir dynamics and parameters that affect CO_2 mineralization. Understanding these parameters is critical to maximizing the amount of CO_2 mineralized in the subsurface. One of the most challenging parameters to determine is the reactive surface area (RSA) which is the exposed area

of the reactive minerals that to the pore space and in contact with fluids insides and will contribute to releasing cations after CO_2 injection. RSA can be determined experimentally using micro-imagining techniques or mathematically estimated using a mineral's specific surface area (SSA). Accurate estimation of RSA is very important to build a reactive transport model to predict the chemical and physical changes in the pore space during CO_2 sequestration (Beckingham et al. 2016).

Luo et al. (2012) studied the effect of changing the RSA on CO_2 sequestration through mineral trapping. Their study assumed that the reactive reservoir minerals are calcite, anorthite, and kaolinite. In the study, seven cases of CO_2 sequestration were simulated. In each case, the RSA of calcite and anorthite is changed by changing the mineral grain diameter, where the RSA decreases with increasing grain size. The amount of CO_2 mineralized is higher at high RSA, as shown in Figure 2-12. It is observed at the end of the simulation that the amount of CO_2 dissolved in brine is higher as the RSA decreases. In the cases of high RSA, more cations will be released from the reactive minerals to the solution to react with dissolved CO_2 and precipitate as carbonate minerals. Thus, there will be less CO_2 dissolved in brine at the end of the simulation because the CO2 mineralization process consumes it. Consequently, it is observed that the pH of brine is much lower in the cases of low RSA due to the higher concentration of hydrogen ions that were not consumed by mineral dissolution reactions.

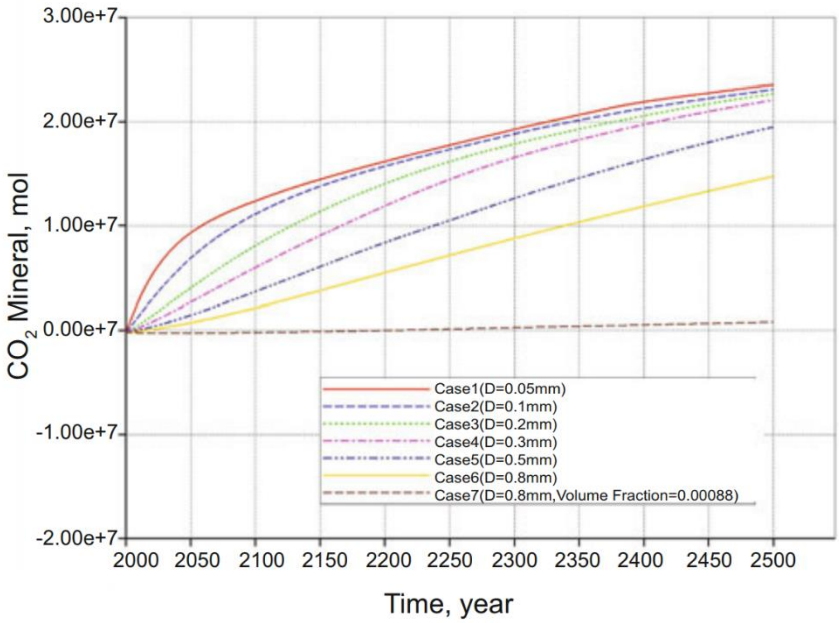

Figure 2-12. CO_2 mineralization decreases with decreasing the reactive surface area (RSA). D: the grain diameter that is used to calculate RSA (Luo et al. 2012).

Zhang and DePaolo (2017) studied the CO_2 mineralization rate in volcanic sandstone as a function of rock mineralogy, pH, and brine fluid velocity in the reservoir using three different data sets. The objective is to find a fractional CO_2 mineralization rate per year. The amount of CO_2 mineralized depends on the amount of cations released from the reactive minerals and the fraction volume of reactive minerals concerning the rock bulk volume. The number of cations minerals released depends on the initial pH of the brine and how quickly the brine flow in the formation after CO_2 injection. If the pH is more than four and the plume velocity is bigger than five m/year, the cations release rate ranges between 0.01 to 10^{-4} per year in fraction (Zhang and DePaolo 2017). The fractional cations release rate is expressed by the following equation:

$$\mathrm{R_{fractional}}(\mathrm{yr^{-1}}) = \frac{(\mathrm{Ca + Mg + Fe})_{\mathrm{si,released}}}{\Delta \mathrm{t} \sum(\mathrm{Ca + Mg + Fe})_{\mathrm{si,rock}}} \qquad \mathrm{Eqn.}\ 2-1$$

The fractional release rate is a function of the total amount of cations released divided by the initial cations inside the formation rock multiplied by the time of the process. The number of cations released is a reflection of mineral dissolution. Figure 2-13 shows the effect of the pH of the mineral dissolution rate constant and the time required to dissolve 1 mm of that mineral. The change in pH due to CO_2 dissolution in brine is observed mainly near the wellbore. This is because most of the CO_2 is dissolved in brine near the wellbore and takes a long time to migrate to the rest of the reservoir (Zhang and DePaolo 2017).

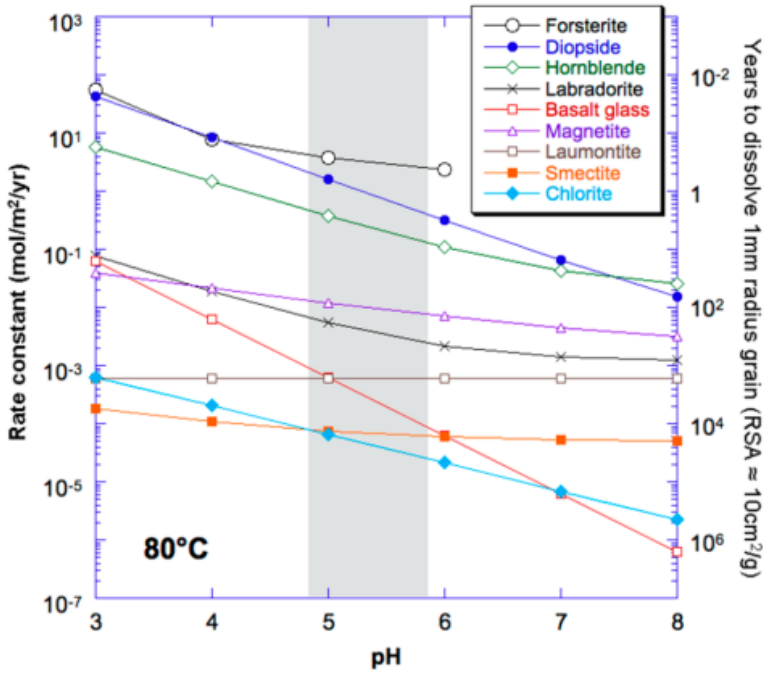

Figure 2-13. The rate of mineralization is higher at lower pH values (Zhang and DePaolo 2017).

The potential of mineralizing CO_2 in a reservoir is determined by the amount of CO_2 dissolved in brine and the amount of CO_2 gas that exists in the pore space with divalent cations released from mineral dissolution. The mineralization potential of CO_2 in a reservoir is expressed by the following equation:

$$E_{MT} = \frac{(1-\emptyset)\, X_{rm}\, \rho_{rm} M_{CO_2}}{\emptyset \left[s_g + (1-s_g) S_b \right] \rho_{CO_2} M_{rm}} \qquad \text{Eqn. } 2-2$$

Where X_{rm} is the reactive mineral volume fraction in the formation, Ø is the initial porosity, ρ is density, M is molar weight, S_g is gas saturation at the end of injection, and S_b is CO_2 volumetric solubility in brine. The study showed that the mineralization potential is small in volcanic sedimentary formation due to the small fraction of reactive minerals. Thus, mineralizing all the injected CO_2 in sedimentary formations takes hundreds of years. Finally, Zhang and DePaolo (2017) concluded the study by introducing the equation for CO_2 mineralization rate in fractions per year as follows:

$$\text{Minerlization Rate } (yr^{-1}) = \frac{(1-\emptyset)\, X_{rm}\, \rho_{rm} M_{CO_2}}{\Delta t_{min}\, \emptyset \left[s_g + (1-s_g) S_b \right] \rho_{CO_2} M_{rm}}$$

$$= \frac{N_{cations}}{\Delta t_{min} N_{CO_2}} \qquad \text{Eqn. } 2-3$$

Where N is the number of moles that exist in the pore space once the injection stope and t_{min} is the mineralization time.

Xiong et al. (2018) conducted an experiment on CO_2 sequestration using naturally porous basalt core samples obtained from the Grand Ronde formation. This formation is located in eastern Washington, where a pilot-scale CO_2 sequestration was conducted by injecting 1000 tonnes of CO_2. The objective of the study was to quantify the CO_2 mineralization rate and the type of mineral deposits. The core composition is 58% plagioclase, 14% pyroxene, 3% ilmenite, and 5% glass. They found that the carbonate minerals precipitated after 20 weeks as aragonite and calcite. Calcite and aragonite are calcium carbonates, but it was observed that calcium forms under lower temperatures and lower Mg:Ca ratios.

On the other hand, aragonite precipitate more under higher temperatures and higher Mg:Ca ratio. In addition, calcite is more favorable to form at higher pH than 5. It is observed that the majority of CO_2 was deposited around the fractures; however, after 40 weeks, carbonate minerals were formed in pores that have no clear connection with the fractures indicating that dissolved CO_2 flew through diffusion to these areas. Figure 2-14 shows the precipitation profile and history. The carbonation rate is controlled by supersaturation and nucleation conditions. No carbonate minerals are observed in the core basalt sample due to the low saturation of cations. Mineral precipitation occurred after 20 weeks because the solution in fractures and pores was supersaturated with calcium ions released from the mineral dissolution. Carbonate minerals occupied 13% of the fracture volume after 40 weeks. The CO_2 mineralization rate was estimated to be 1.24 ± 0.52 kg per m^3 of basalt per year. Thus, the injected CO_2 into Grand Ronde basalt will be completely mineralized at this rate after approximately 40 years (Xiong et al. 2018).

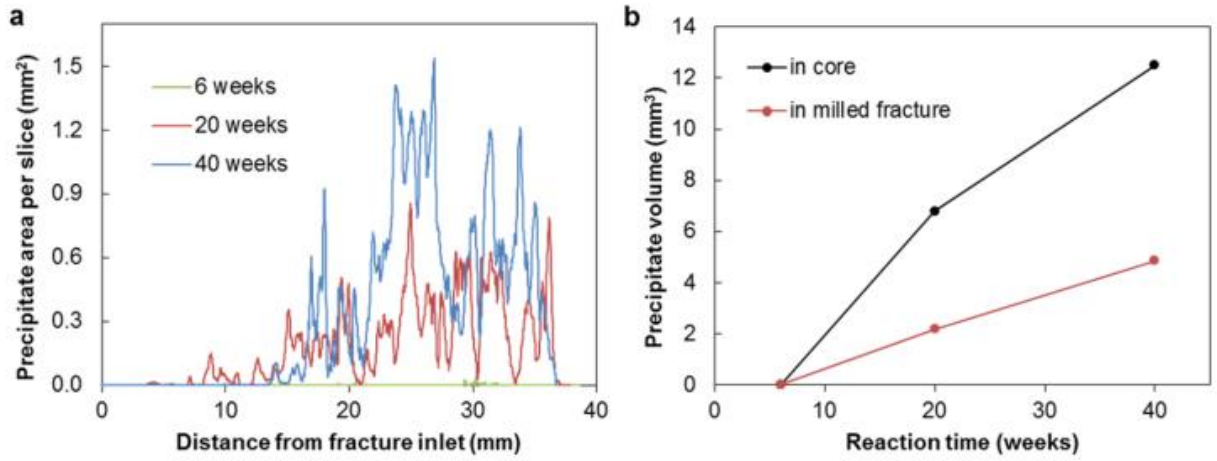

Figure 2-14- most of CO_2 mineralization occurs away from the fracture inlet.

André et al. (2007) conducted a numerical modeling to simulate CO_2 storage in the Dogger aquifer in Paris Basin in France. The study included studying the difference between injecting supercritical CO_2 and CO_2-saturated water. The mineralogy of the aquifer included 70% calcite,

10% dolomite, 5% siderite, 5 % illite, 5% Albite, and 5% K-feldspar. The most reactive minerals with dissolved CO_2 are calcite, dolomite and siderite which react as follows:

$$\text{Caclite} + H^+ \leftrightarrow HCO_3^- + Ca^{2+}$$

$$\text{Dolomite} + 2H^+ \leftrightarrow 2HCO_3^- + Ca^{2+} + Mg^{2+}$$

$$\text{Siderite} + H^+ \leftrightarrow HCO_3^- + Fe^{2+}$$

In the case of injecting CO_2-saturated water, 70% calcite, %10 dolomite, and 5% siderite were dissolved in solution near the wellbore which resulted in a significant increase in porosity by 90% approximately. 10 m away from the injection well, the porosity increased by 70% approximately. There was no change in the porosity in zones that are around 30 meters away from the injection well. Thus, injecting CO_2-saturated water will highly damage the reservoir near the injection well. On the other hand, injecting supercritical CO_2 will damage the formation as much. The injection of supercritical CO_2 creates three regions around the wellbore with different fluid phases. The first region is called the dry-out zone, which is located directly around the wellbore, where all the water has been displaced by supercritical fluid. The residual water saturation will evaporate over time, leading to salt deposits near the wellbore, reducing porosity. André et al. (2007) observed the precipitation of anhydrite and dolomite in the dry-out zone that reduced porosity by 1%. The second zone is the two-phase zone, where supercritical CO_2 reacts and dissolves in water. This zone will experience pH reduction that will lead to the dissolution of reactive minerals to react with carbonate ions, increasing the solution pH and precipitating minerals. This simulation observed that the dissolution rate of calcite, dolomite, and siderite is much higher than the precipitation rate of illite precipitation, which increased the porosity by 2.5% maximum in the second zone. The third region is the undisrupted zone, where it is fully

saturated with brine and retains the initial conditions before CO_2 injection. Thus, this zone didn't have geochemical reaction or change in porosity (André et al. 2007). Figure 2-15 shows a cross-section profile of the geochemical reactions that occur around the wellbore after injecting supercritical CO_2.

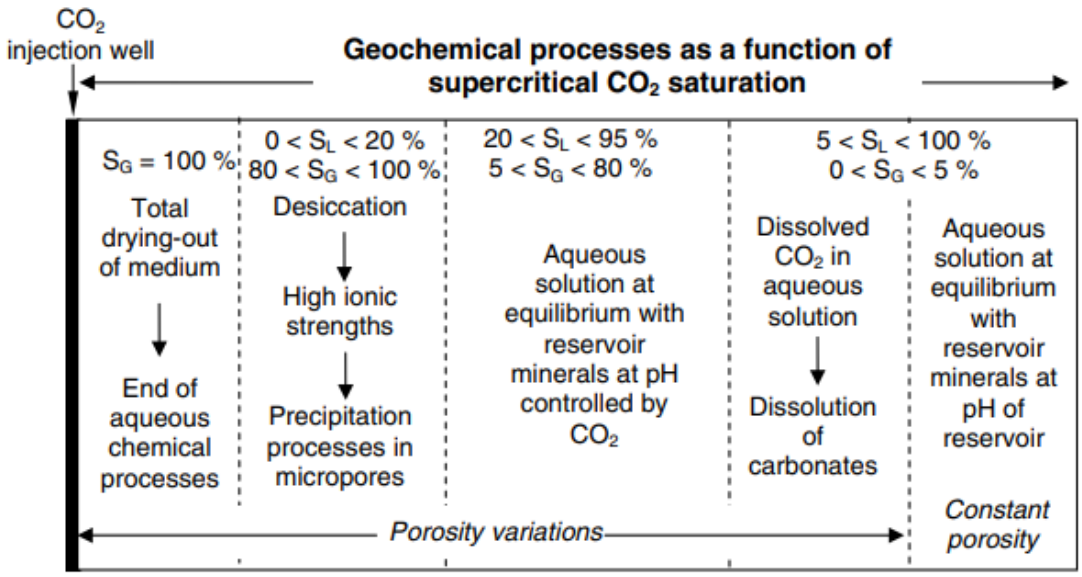

Figure 2-15. Porosity alteration occurs around the wellbore due to the dry-out effect near the wellbore and due to CO2 mineralization in the other zones (André et al. 2007).

Postma et al. (2022) studied the influence of porosity, permeability, reservoir dip angle, and accessible surface area on the dynamics of mass transport and CO_2 mineralization in basalt. Injecting CO_2-saturated water into a saline aquifer divides the aquifer into three compartments: the brine region, the mobile CO_2 region, and the residual CO_2 region. These three regions are formed after the injection period ends due to the buoyance effect, where brine has the highest density, followed by residual CO2 and then mobile CO_2. Three primary minerals were included in this study: 15% olivine, 15% pyroxene, and 15% plagioclase. The results show that the rate of CO_2 mineralization is controlled by the CO_2 mass transfer among the three regions. CO_2

transfers through the partition between the mobile and residual regions and by convection mixing with the brine region.

The convection mixing between the brine and CO_2 regions will cause a downward mass transport of dissolved CO_2 into the brine due to the higher density. This mass transfer is controlled by permeability, porosity, and dip angle. The mineralization rate increases with increasing permeability and dip angle and decreasing porosity. High permeability enhances the flow and the mixing between the brine and CO_2-saturated. Likewise, increasing the dip angle increases the interface area between the brine region and the CO_2-saturated region, enhancing the mass transfer of CO_2. Lower porosity enhanced the convection mixing between the brine and CO_2 regions. In addition, the study concluded that injecting CO_2-saturated water instead of supercritical CO_2 leads to quicker mineralization and pressure build-up (Postma et al. 2022).

Postma et al. (2022) also investigated the change in porosity and permeability due to mineral saturation. The results show that both permeability and porosity decreased due to CO_2 mineralization. Postma et al. (2022) suggested that the change in permeability can be estimated through porosity change as follows:

$$\mathrm{K} = \mathrm{K}_{\mathrm{init}} \frac{(1 - \emptyset_{\mathrm{init}})^2}{\emptyset_{\mathrm{init}}^3} \frac{\emptyset^3}{(1 - \emptyset)^2} \qquad \mathrm{Eqn.}\, 2 - 4$$

A smiler study by Jiang and Tsuji (2014) investigated the change in porosity and permeability due to mineralization. The study found that most CO_2 mineralization occurs mostly in smaller pores. Like previous studies, they found that both permeability and porosity were reduced due to CO_2 mineralization. In addition, relative permeability reduction in the non-wetting phase after CO_2 mineralization was much higher than the wetting phase relative permeability (Jiang and Tsuji 2014).

Li et al. (2018)conducted a study to investigate the effect of impurities such as O_2 and N_2 in the geological storage of CO_2. In the same, the effect of pressure and temperature in mineral dissolution in water of CO_2 injection was investigated as well. In pure water, the mineral dissolution is higher with temperature while in a CO_2 saturated fluid, mineral dissolution is lower at higher temperatures due the effect of CO_2 solubility in water as a function of temperature.

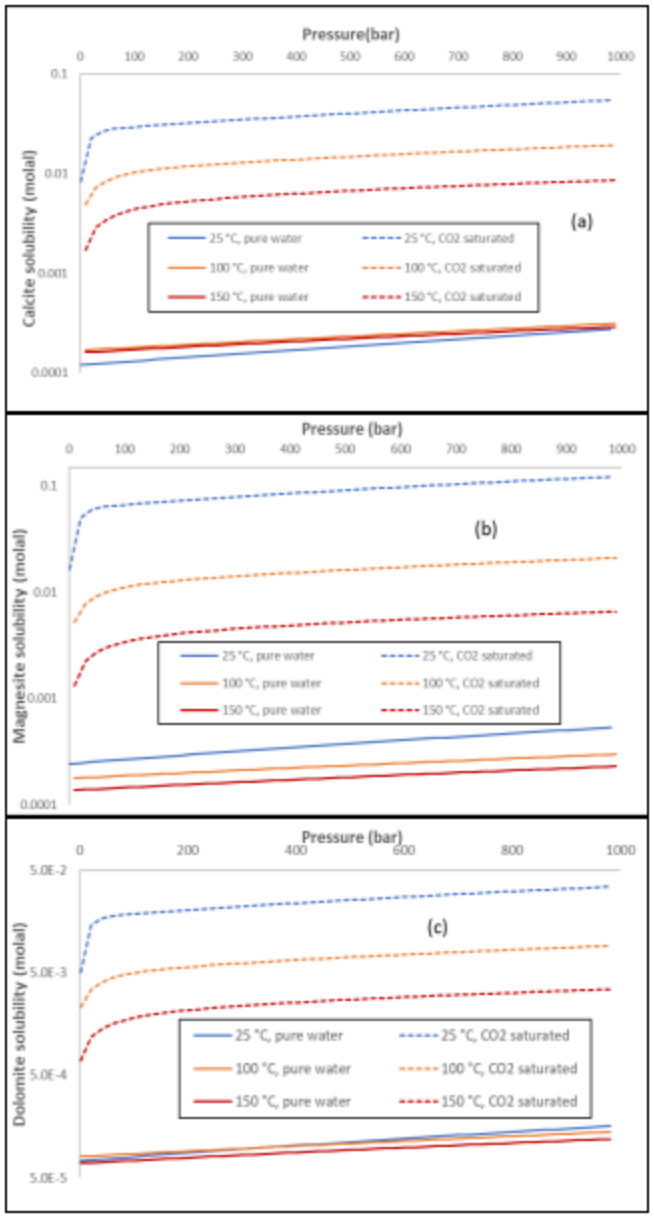

Figure 2-16- Mineral dissolution is CO_2 saturated water is lower at higher temperatures (Li et al. 2018).

Figure ***2-16*** shows the mineral dissolution as a function of pressure and temperature in pure water and CO_2 saturated water.

The key observations on CO_2 mineralization can be summarized as follows:

- CO_2 dissolution in brine leads to a lower pH of the solution.
- Hydrogen produced from CO_2 dissolution will attack the surface of the minerals leading to the release of divalent cations and lower the pH of the solution.
- Divalent cations react with the carbonate ions to mineralize in the form of carbonate minerals.
- The number of cations released depends on the minerals' reactivity and the reactive surface area.
- The injection of CO_2-saturated water will result in faster mineralization than supercritical CO_2, but it will also damage the formation significantly.
- Mineral dissolution and precipitation occur after CO_2 injection; thus, the increases or decreases in porosity and permeability will depend on the net change of the volume of the mineral in the pore space.
- Most of the mineralization occurs in the regions near the wellbore.

Chapter 3 - Solubility of CO_2 in Brine

3.1. Overview

Understanding CO_2 solubility in brine is critical to understanding reservoir dynamics after CO_2 injection. To mineralize CO_2 into carbonate minerals, CO_2 first must dissolve in the brine to form hydrogen and bicarbonate ions that will trigger the motion toward CO_2 mineralization. The amount of CO_2 dissolved in brine is controlled by pressure, temperature, and salinity (Wang et al. 2013). Upon the injection of CO_2, the reservoir fluid system changes from one fluid phase system to a two-fluids phase system. The dissolution of CO_2 will continue until a new chemical equilibrium in the reservoir is reached. The injected CO_2 will form a gas cap before dissolving water. In this gas cap, gas CO_2 has a higher chemical potential than the aqueous CO_2 in the liquid phase. This imbalance will cause CO_2 molecules from the gas phase to dissolve in water a become aqueous CO_2 as follows:

$$CO_2(g) \leftrightarrow CO_2\ (aq)$$

Chemical equilibrium will be reached once the chemical potential of gas and the aqueous phase of CO_2 are equal. Chemical potential is a function of Gibbs free energy which is a function of enthalpy and entropy, Equation 1 and equation 2, respectively.

$$\mu_i = \left(\frac{\partial G}{\partial n_i}\right)_{p,T,n_j \neq i} \qquad \text{Eqn. } 3-1$$

$$\Delta G = \Delta H - T\Delta S \qquad \text{Eqn. } 3-2$$

Where μ is the chemical potential, G is Gibbs free energy, n is the number of moles, H is the enthalpy and S is the entropy.

Th dissolution of CO_2 into water happens when the change of Gibbs free energy is negative. From Equation 1, the dissolution is water will occur if the change in entropy is positive or the change in enthalpy is negative. Upon the injection of CO_2, the entropy of CO_2 in the gas phase is higher than in the aqueous phase; thus, to make the change in Gibbs energy negative, the change enthalpy must be negative, which means the reaction must be exothermic as follows:

$$CO_2(g) + H_2O\ (l) \leftrightarrow CO_2(aq) + H_2O\ (aq) + energy$$

The chemical potential of a chemical component can be expressed in terms of fugacity and activity coefficient. The injection of CO_2 into a reservoir changes the partial pressure and the concentration of CO_2 and water molecules in the vapor and liquid. In an ideal system, fugacity is equal to partial pressure. If a system for CO_2 sequestration is assumed to be closed, isothermal and constant in volume, the change in potential energy can be rewritten as follows:

$$dG = dH - SdT \qquad Eqn.\ 3-3$$

$$H = U + PV \qquad Eqn.\ 3-4$$

$$dH = dU + PdV + VdP \qquad Eqn.\ 3-5$$

$$dG = dU + PdV + VdP - SdT \qquad Eqn.\ 3-6$$

Where U is the internal energy of the system. In an isothermal, constant volume, and closed system, the change in temperature, volume, and internal energy is zero, thus:

$$dG = VdP \qquad Eqn.\ 3-7$$

$$dG = \frac{nRT}{P} dP \qquad \text{Eqn. } 3-8$$

Thus, for an ideal gas, the chemical potential is expressed as follows:

$$d\mu = d\bar{G} = RT\, d(\ln P) \qquad \text{Eqn. } 3-9$$

$$\mu\,(T,P) = \mu^0(T) + RT \ln\left(\frac{P}{P_0}\right) \qquad \text{Eqn. } 3-10$$

Where $\bar{G}$ is the molar Gibbs free energy, and μ^0 is the standard Gibbs free energy.

In a reservoir system, mixing CO_2 ions with water ions in the vapor and aqueous phases is not ideal. Thus, the parameter fugacity and activity are used instead of pressure in real mixtures to calculate the potential energy of a component in the vapor and liquid phases, respectively. The chemical potential of component i in the vapor phase and liquid phase in expressed as follows:

$$\mu_i^v\,(T,P) = \mu^{v0}(T) + RT \ln(f_i) \qquad \text{Eqn. } 3-11$$

$$\mu_i^l\,(T,P) = \mu^{v0}(T) + RT \ln(a_i) \qquad \text{Eqn. } 3-12$$

Where f_i and a_i are the fugacity and activity of component i.

The dissolution of CO_2 in the water will continue until the chemical potential of CO_2 in the vapor and liquid phases are equal. The solubility of CO_2 in water at a specific pressure and temperature condition can be estimated using Henry's law. Equation 13 shows Henry's law, where the solubility of the dissolved gas concentration is a function of the partial pressure of the gas.

$$C = kP_{gas} \qquad \text{Eqn. } 3-13$$

Where C is the gas solubility, k is Henry's law constant, and P_{gas} is the partial pressure of the gas. Henry's law constant is specified experimentally or determined empirically as a function of pressure, temperature, and component molar volume.

Next section will investigate CO2 solubility in water as a function of pressure, temperature and salinity using Chang et al. (1996) and Duan and Sun (2003) models. In addition, other models and case studies of CO_2 solubility will be investigated and summarized.

3.2. CO_2 solubility models and Key Findings

Duan and Sun (2003) developed a model to predict CO_2 solubility in water at different pressure, temperature, and ionic strength. The model is developed by equating the chemical potential of CO_2 in the vapor phase to the chemical potential of CO_2 in the liquid phase. The model is sufficient to predict CO_2 solubility at temperatures between 273 to 533 K, pressures between 0 and 2000 bar, and ionic strength up to 4.3 m. The ionic strength reflects salt concentration in the water in moles per kg of water. The model predicts CO_2 solubility with an 7% uncertainty. Duan rt al model of solubility is expressed as follows:

$$\ln \frac{y_{CO_2} P}{m_{CO_2}} = \frac{\mu_{CO_2}^{l(0)}(T,P) - \mu_{CO_2}^{v(0)}(T)}{RT} - \ln \varphi_{CO_2}(T,P,y) + \ln \gamma_{CO_2}(T,P,m) \qquad \text{Eqn. } 3-14$$

Where $\mu_{CO_2}^{l(0)}$ is CO_2 chemical potential in the liquid phase at unit molarity, $\mu_{CO_2}^{v(0)}$ is CO_2 chemical potential in the vapor phase at the pressure of 1 bar, φ_{CO_2} is CO_2 fugacity coefficient, γ_{CO_2} is CO_2 activity coefficient and y_{CO_2} is the CO_2 mole fraction in the vapor phase. y_{CO_2} is calculated by assuming that the vapor pressure of water in mixtures is equal to the saturation pressure of pure water, thus, y_{CO_2} is calculated as follows:

$$y_{CO_2} = \frac{P - P_{H_2O}}{P} \qquad \text{Eqn. } 3-15$$

Where P_{H_2O} is pure water saturation pressure. Equation 14 is further modified by introducing parameterization parameters to estimate the activity coefficient as follows:

$$\ln \gamma_{CO_2} = \sum_c 2\lambda_{CO_2-c}\, m_c + \sum_a 2\lambda_{CO_2-a}\, m_a + \sum_c \sum_a \xi_{CO_2-a-c}\, m_c m_a \qquad \text{Eqn. } 3-16$$

$$\ln \frac{y_{CO_2} P}{m_{CO_2}} = \frac{\mu^{l(0)}_{CO_2}(T,P)}{RT} - \ln \varphi_{CO_2}(T,P,y) + \sum_c 2\lambda_{CO_2-c}\, m_c + \sum_a 2\lambda_{CO_2-a}\, m_a + \sum_c \sum_a \xi_{CO_2-a-c}\, m_c m_a \qquad \text{Eqn. } 3-17$$

Where λ is a second-order interaction parameter and ξ is a third-order interaction parameters that are estimated numerically.

Chang et al. (1996) developed a model to simulate CO_2 flooding in oil and gas reservoirs in which CO_2 solubility in water plays a critical part. Chang et al. (1996) developed a correlation to estimate CO_2 solubility in distilled water. The model is expressed as follows:

$$R_{sw} = a \,.\, p \,.\, \left[1 - b.\sin\left(\frac{\pi}{2}.\frac{c \,.\, p}{c \,.\, p + 1}\right)\right] \text{ if } p < p^0 \qquad \text{Eqn. } 3-18$$

$$R_{sw} = R^0_{sw} + m \,.\, (p - p^0) \text{ if } p \geq p^0 \qquad \text{Eqn. } 3-19$$

Where R_{sw} is CO_2 solubility in water in SCF/BBL, p is pressure in psia. a, b, c, m and p^0 are estimated as follows:

$$a = \sum_{i=0}^{4} a_i . 10^{-3i} . T^i \qquad \text{Eqn. } 3-20$$

$$b = \sum_{i=0}^{4} b_i . 10^{-3i} . T^i \quad 0 < b < 1 \qquad \text{Eqn. } 3-21$$

$$c = 10^{-3} . \sum_{i=0}^{4} c_i . 10^{-3i} . T^i \qquad \text{Eqn. } 3-22$$

$$p^0 = \frac{2}{\pi} . \frac{\sin^{-1} b^2}{c . \left[1 - \frac{2}{\pi} . \sin^{-1} b^2 \right]} \qquad \text{Eqn. } 3-23$$

$$R_{sw}^0 = a . p^0 . (1 - b^3) \qquad \text{Eqn. } 3-24$$

$$m = a \left\{ 1 - b \left[\sin\left(\frac{\pi}{2} . \frac{c . p^0}{c . p^0 + 1} \right) \right] + \frac{\pi}{2} . \frac{c . p^0}{(c . p^0 + 1)^2} \cos\left(\frac{\pi}{2} . \frac{c . p^0}{c . p^0 + 1} \right) \right\} \qquad \text{Eqn. } 3-25$$

Where T is temperature and a_i, b_i and c_i are coefficients shown in Table 3-1. The above correlation is modified to estimate CO_2 solubility in brin as follow:

$$\log\left(\frac{R_{sb}}{R_{sw}} \right) = -0.028 . C . T^{-0.12} \qquad \text{Eqn. } 3-26$$

Where R_{sb} is CO_2 solubility in brine, and C is brin salinity.

Table 3-1. coefficients that are used to calculate a, b, and c in CO2 solubility model of

	$i = 0$	$i = 1$	$i = 2$	$i = 3$	$i = 4$
a_i	1.163	−16.630	111.073	−376.859	524.889
b_i	0.965	−0.272	0.0923	−0.1008	0.0998
c_i	1.280	−10.757	52.696	−222.395	462.672

Spycher et al. (2003) developed a model to predict the solubility of CO_2 in water at temperature range of 12 to 100 ℃ and pressure up to 600 bar. The model was developed specifically to

understand the dissolution of CO_2 in water during the geological sequestration process. This model is also derived from equating the chemical potential of different competent in the vapor and liquid phases. The model is expressed as follows:

$$x_{co2} = B\left(1 - y_{H_2O}\right) \qquad \text{Eqn. } 3-27$$

Where x_{co2} is the molality of CO_2 in the aqueous phase and y_{H2O} is water fraction in the gas phase which can be estimated as follows:

$$y_{H_2O} = \frac{1 - B}{\frac{1}{A} - B} \qquad \text{Eqn. } 3-28$$

Where A and B are parameters that are estimated as follows:

$$A = \frac{K^0_{H_2O}}{\emptyset_{H_2O} P_{tot}} \exp\left(\frac{(P - P^0)\overline{V_{H_2O}}}{RT}\right) \qquad \text{Eqn. } 3-29$$

$$B = \frac{\emptyset_{CO_2} P_{tot}}{55.508\, K^0_{CO_2}} \exp\left(-\frac{(P - P^0)\overline{V_{CO_2}}}{RT}\right) \qquad \text{Eqn. } 3-30$$

Where K_{H2O} is the equilibrium constant of water, K_{CO2} is the equilibrium constant of CO_2, P is the pressure, $\bar{V}$ is the partial molar volume, R is the gas constant, T is temperature and Ø is the fugacity coefficient.

Figure 3-1 to Figure 3-5 show the CO_2 solubility as a function of pressure and salinity at different temperatures using Duan and Sun (2003) model and Chang et al. (1996) model. From the figures, CO_2 solubility increases as the pressure increases and decreases as the salinity and temperature increases.

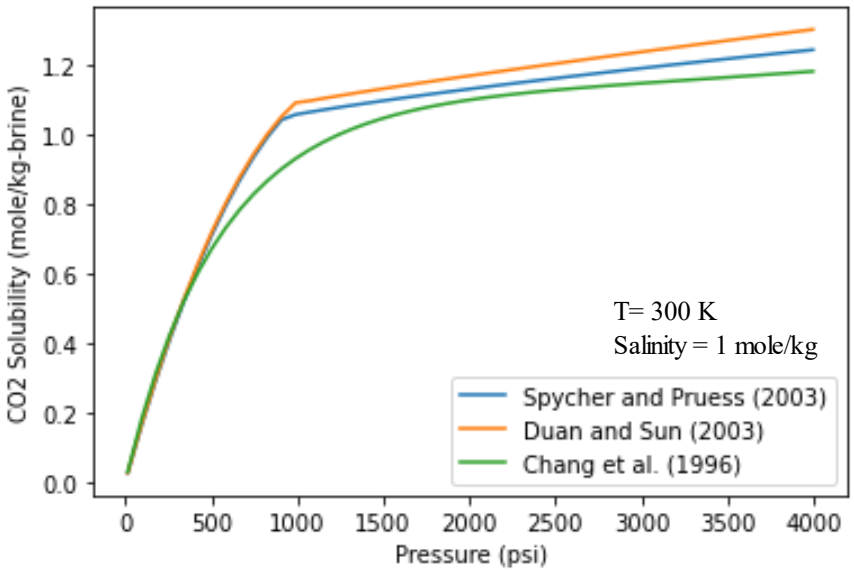

Figure 3-1. CO_2 solubility as a function of pressure at constant temperature of 300 K and constant salinity of 1 mol/kg-H2O. All models show that CO_2 solubility increases with pressure.

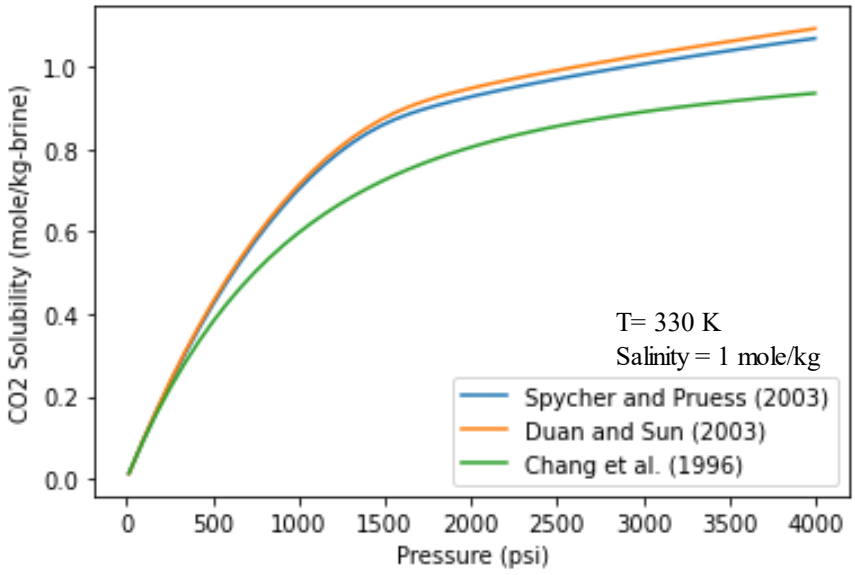

Figure 3-2. CO_2 solubility as a function of pressure at constant temperature of 330 K and constant salinity of 1 mol/kg-H2O. All models show that CO_2 solubility increases with pressure. CO_2 solubility is lower at 330 K than 300 K. Thus, CO_2 solubility decreases with temperature.

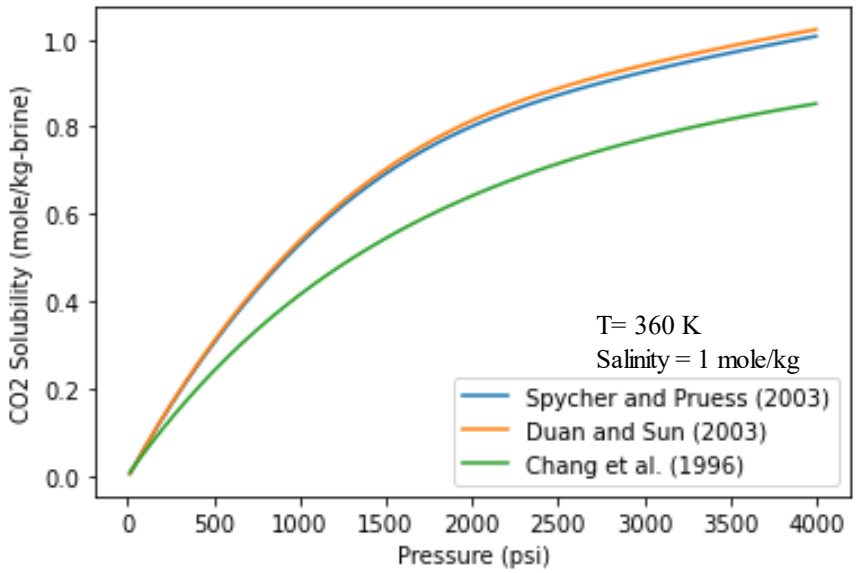

Figure 3-3. CO_2 solubility as a function of pressure at constant temperature of 360 K and constant salinity of 1 mol/kg-H2O. All models show that CO_2 solubility increases with pressure. CO_2 solubility is lower at 360 K than 330 K. Thus, CO_2 solubility decreases with temperature.

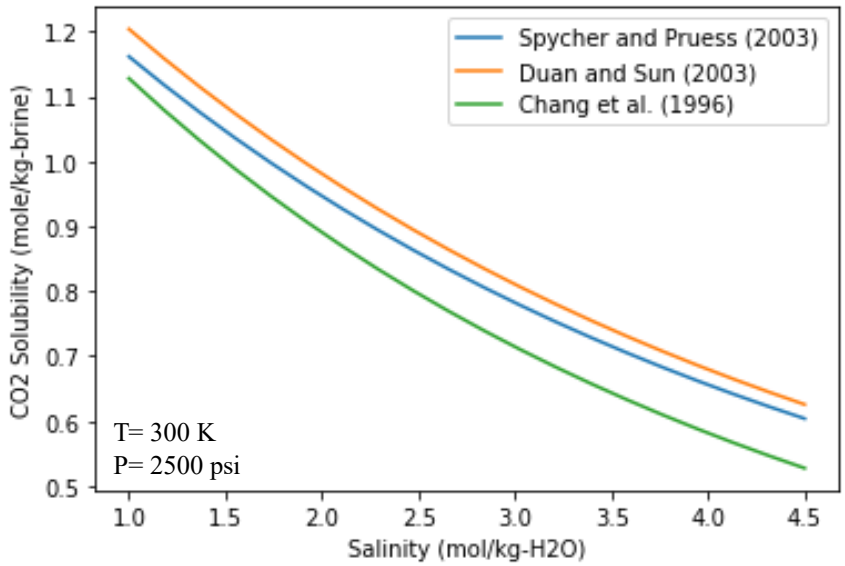

Figure 3-4. CO_2 solubility as a function of salinity at constant temperature of 330 K and constant pressure of 2500 psi. All models show that CO_2 solubility decreases with salinity.

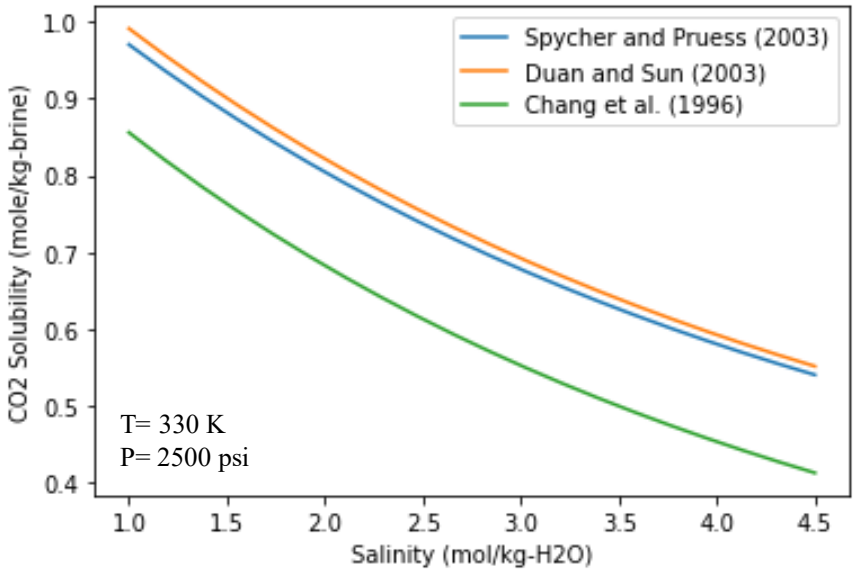

Figure 3-6. CO_2 solubility as a function of salinity at constant temperature of 330 K and constant pressure of 2500 psi. All models show that CO_2 solubility decreases with salinity. CO_2 solubility is lower at 330 K than 300 K. Thus, CO_2 solubility decreases with temperature.

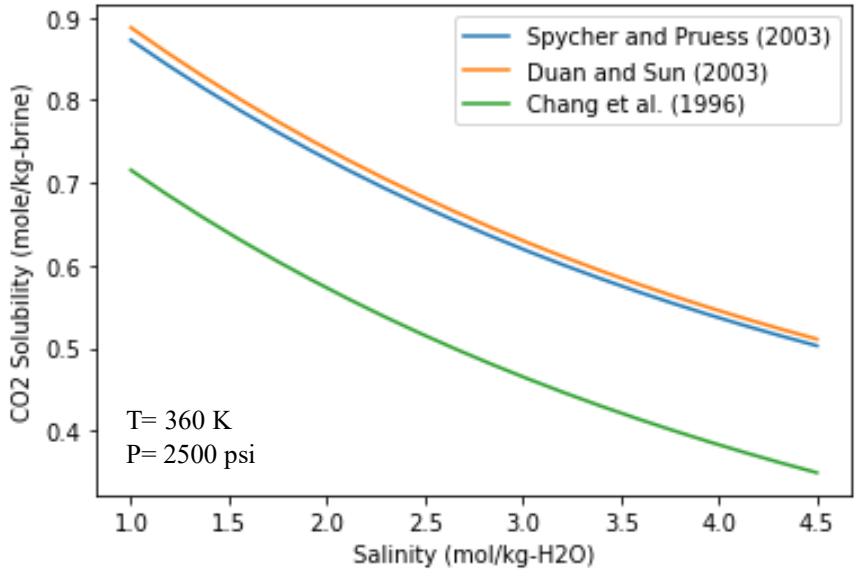

Figure 3-5. CO_2 solubility as a function of salinity at constant temperature of 330 K and constant pressure of 2500 psi. All models show that CO_2 solubility decreases with salinity. CO_2 solubility is lower at 360 K than 330 K. Thus, CO_2 solubility decreases with temperature.

Sadeghi et al. (2015) conducted a comprehensive study to compare experimental CO_2 solubility in brine with an analytical neural network model and a thermodynamic-based model. The thermodynamic model is designed by coupling Redlich-Kwong EOS with Pitzer expansion to calculate CO_2 fugacity and activity in the CO_2-rich phase. The neural network model is developed by training and testing the CO_2 solubility dataset using a two-layer arrangement with five neurons. The neural network is designed to combine accuracy and low computation cost. The results show that experimental CO_2 solubility has a good machine with both thermodynamic and neural network models. CO_2 solubility increases with pressure; however, at high pressure, CO_2 becomes liquid, and dissolution in water decreases. The study shows that experimental and estimated CO_2 solubility decreases with temperature and salinity. Fig shows a comparison between experimental CO_2 solubility in brin and compared thermodynamic-based model and neural network model.

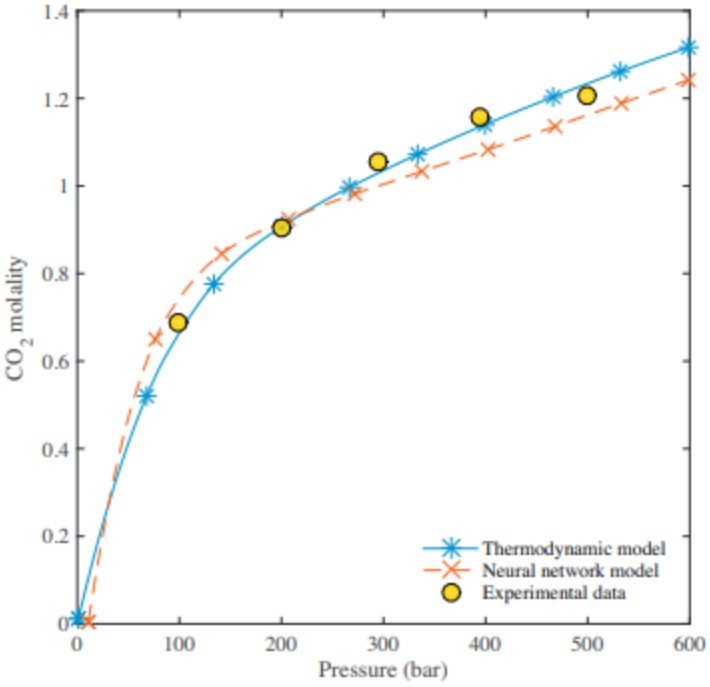

Figure 3-7. Estimated and experimental CO_2 solubility as function of pressure. The change in the slope indicated the phase change of CO2 to liquid (Sadeghi et al. 2015).

Chapter 4 - Modeling CO_2 mineralization in Mafic basaltic formation

4.1. Base Model

A. Static Model Description

A 3D numerical reservoir model was built to address the following CO_2 trapping mechanisms in a basalt formation: structural trapping, residual trapping, solubility trapping, and mineralization. In particular, the main interest is the permanent trapping of CO_2 through mineralization. The model is designed to simulate the chemical reactions between the injected supercritical CO_2 and the saline water in the reservoir. The maximum reservoir pressure is mentored to be 90% of fracture pressure to avoid any risk of fracturing the reservoir and follow EPA regulations for Class VI well (U.S. EPA 2018). CO_2 is injected at a constant rate of 200 MCF/day for 4 years. The reservoir model has a uniform porosity and permeability distribution with a total pore volume of 4.86×10^6 ft^3. As shown in Figure 4-1, the reservoir is divided into 15 layers with a total thickness of 225 ft. The lower 5 layers are perforated for CO_2 injection. The total simulation period is 200 years. The model is designed to be a closed boundary system in all directions in such that there is no water influx or efflux after CO_2 injection. Likewise, water vaporization is neglected during the simulation. The reservoir model inputs are shown in Table 4-1

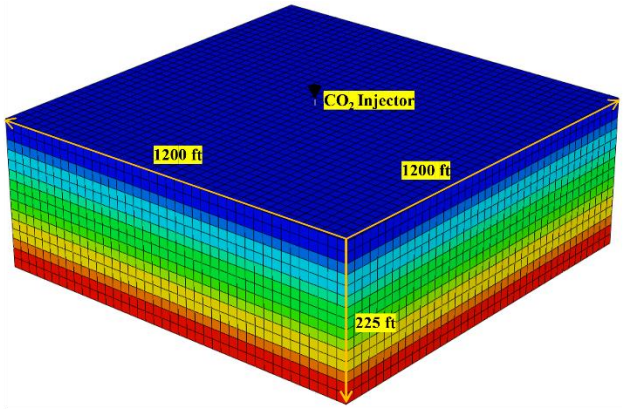

Figure 4-1. The reservoir model is designed with 15 layers with a total depth of 225 ft. The injection well is centered in the middle of the model and will inject 200 MCF/day for 4 years.

Table 4-1. Reservoir static model inputs.

Input	Specifications
N_x, N_y, N_z	40, 40, 15
D_x, D_y, D_z	30 ft * 30 ft * 15 ft
Porosity	15%
Permeability in x direction	100 md
Permeability in y direction	100 md
Permeability in z direction	10 md
Formation top	4500 ft
Initial pressure	1950 psi
Temperature	123 F
Initial injection rate	200 MCF/day
Water saturation	100%
Fracture pressure	3600 psi
Maximum allowable pressure	3240 psi
Salinity	80000 ppm

B. Structural and Residual Trapping Modeling

Structural trapping is obtained by setting the upper layer as a closed boundary in which CO_2 will accumulate if it reaches the top of the model. Residual trapping will occur due to the relative permeability hysteresis effect. CO_2 will displace water in the pore space during the injection. As CO_2 migrates upward due to gravity segregation, the imbibition process starts where brine reoccupies the pore space and residually traps some CO_2 particles. CO_2 will not migrate immediately in the reservoir after injection. CO_2 saturation in the pore space must reach the critical gas saturation to strati migrating in the reservoir. CO_2 residual saturation is modeled using Land (1968) correlation, Equation 4-1. The amount of CO_2 that will be residually trapped

in a pore space increases with the increase of the historical gas saturation and decreases with the increase of critical gas saturation. The relative permeabilities of CO_2 and brine as a function of water saturation are collected from Kumar et al. (2005) and plotted as shown in Figure 4-2.

$$S_{grh} = \frac{S_{gh} - S_{gcrit}}{1 + C(S_{gh} - S_{grit})} \qquad \text{Eqn. } 4-1$$

Where S_{grh} is the residual gas saturation, S_{gh} is the maximum hitorical gas saturation and S_{gcrit} is the critical gas saturation. C is a constant and calculated as follows:

$$C = \frac{1}{S_{grmax} - S_{gcrit}} - \frac{1}{S_{gmax} - S_{gcrit}} \qquad \text{Eqn. } 4-2$$

Where S_{grmax} is the maximum gas residual trapping which was set to 40%, S_{gmax} is the maximum possible gas saturation which is 75% as shown in Figure 4-2.

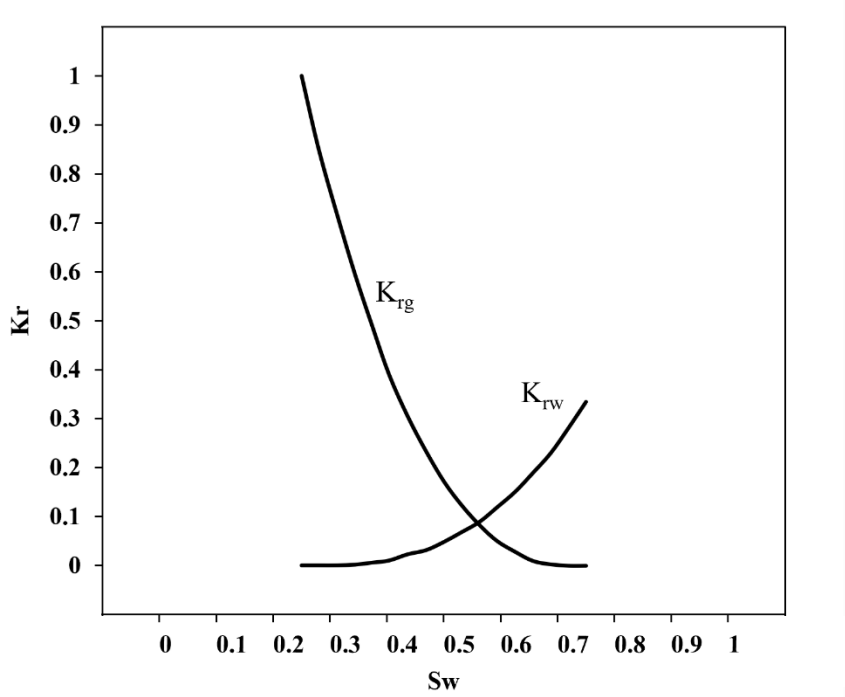

Figure 4-2. Brine and CO2 relative permeability as a function of water saturation. Irreducible water saturation is 25% while critical gas saturation is 25%.

C. Solubility Trapping Modeling

As CO_2 migrates in the reservoir, some CO_2 will dissolve in brine. The dissolution of CO_2 in brine is controlled by pressure, temperature, and salinity. CO_2 solubility is modeled by using Henry's law of fugacity, Equation 4-3. The amount of dissolved CO_2 is proportional to it vapor pressure or in this case, its vapor fugacity. Upon the injection of CO_2, the fugacity of CO_2 in the vapor phase is higher than the fugacity in the aqueous phase. Thus, CO_2 will dissolve in brine until the fugacity equilibrium of CO_2 in vapor and the aqueous phase is reached. Henry law constant (HCO_2) is a function of pressure, temperature, and salinity; however, in the designed model, it only changes due to the change in pressure because temperature and salinity are assumed to be constant throughout the reservoir.

$$f = x_{CO2,w} * H_{CO2} \qquad \text{Eqn. } 4-3$$

To have an accurate estimation of solubility, henry's law constant is modeled using the Harvey (1996) correlation as follows:

$$\ln K_H = \ln P_l^s + \frac{A}{T_r} + \frac{B(1-T_r)^{0.355}}{Tr} + C\exp(1-T_r)\,T_r^{-0.41} \qquad \text{Eqn. } 4-4$$

Where K_H is Henry's law constant, P_l^s is the solvent saturation pressure, T is the reduced temperature, and A, B, and C are tabulated constants. The solvent saturation pressure, which is brine in our model is calculated using Saul and Wagner (1987) as follows:

$$\ln\left(\frac{p}{p_c}\right) = \frac{T_c}{T}\left[a_1\tau + a_2\tau^{1.5} + a_3\tau^3 + a_4\tau^{3.5} + a_5\tau^4 + a_6\tau^{7.5}\right] \qquad \text{Eqn. } 4-5$$

$$\tau = 1 - \frac{T}{T_c} \qquad \text{Eqn. } 4-6$$

Where p is the saturation pressure, p_c is the critical saturation and a_1 to a_5 are tabulated constants.

As shown in Equation 4-4, Henry's law constant is a function of pressure and temperature. To model Henry's law constant as function of salinity, the constant is modified using Cramer (1982) correlation as follows:

$$\log_{10}\left(\frac{H_{salt,i}}{H_i}\right) = k_{salt,i}\, m_{salt} \qquad \text{Eqn. } 4-7$$

Where $H_{salt,i}$ is Henry's law constant of component I in brin, H_i is Henery constant of component i in pure water, $k_{salt,i}$ is component i salting-out coefficient and m_{salt} is brine molality. The salting out coefficient of CO_2 is calculated using Bakker (2003) correlation as follows:

$$k_{salt-CO_2} = 0.11572 - 6.0293 \times 10^{-4}T + 3.5817 \times 10^{-6}T^2 - 3.772 \times 10^{-9}T^3 \qquad \text{Eqn. } 4-8$$

Where T is the temperature in ℃.

D. Mineral Trapping Modeling

In the model, the reservoir formation consists of basalt and wollastonite. Basalt is assumed to be made of three minerals: plagioclase, olivine, and pyroxene. Magnesium endmembers of olivine and pyroxene, and calcium endmembers of plagioclase are used to model the chemical reactions of basalt mineral reactions with hydrogen. The reaction between hydrogen and reservoir minerals will produce magnesium and calcium cations. These cations will react with carbonate ions produced from CO_2 dissolution in the brine, leading to CO_2 mineralization in the form of carbonate minerals, calcite, and magnesite. The initial volume fraction of minerals in the reservoir formation is assumed to be 20% plagioclase, 14% olivine, 14% pyroxene, and 1% wollastonite. The chemical reactions that are included in the model are as follows:

CO_2 dissolution in water

$$CO_2 + H_2O \leftrightarrow H^+ + HCO_3^-$$

$$CO_3^{2-} + H^+ \leftrightarrow HCO_3^-$$

$$H_2O \leftrightarrow H^+ + OH^-$$

Reservoir minerals reactions

$$\text{Anorthite (Plagioclase)} + 8\,H^+ \leftrightarrow 4H_2O + Ca^{2+} + 2\,Al^{3+} + 2\,SiO_2(aq)$$

$$\text{Enstatite (Pyroxene)} + 2\,H^+ \leftrightarrow H_2O + Mg^{2+} + SiO_2(aq)$$

$$\text{Forsterite (Olivine)} + 4\,H^+ \leftrightarrow 2\,H_2O + 2\,Mg^{2+} + SiO_2(aq)$$

$$\text{Wollastonite} + 2\,H^+ \leftrightarrow H_2O + Ca^{2+} + SiO_2(aq)$$

Mineral precipitation (CO_2 mineralization)

$$\text{Calcite} + H^+ \leftrightarrow Ca^{2+} + HCO_3^-$$

$$\text{Magnesite} + H^+ \leftrightarrow Mg^{2+} + HCO_3^-$$

The reaction rates of mineral dissolution and precipitation are modeled using the Transition State Theory (TST), Equation 4-9. The rate constant is a function of temperature, Equation 4-10. However, since the reservoir is assumed to be under isothermal condition, the rate constant will not change during the simulation. Nonetheless, as shown in Figure 4-3, the rate constant is plotted as a function of temperature to understand the temperature effect of the reaction rate which will be discussed further in the sensitivity analysis. The main inputs to simulate these chemical reactions are shown in Table 4-2. According to Beckingham et al. (2016), the reactive surface area (RSA) of a mineral in a rock can be estimated using Equation 4-11. Plagioclase, olivine, and pyroxene RSAs are calculated using Equation 4-11. Calcite RSA is obtained from

Jia et al. (2021) while magnesite RSA is assumed to be equal to calcite RSA. The rest of the input data are collected from Kashim et al. (2020), Schwartz (2022) and Toolbox (2021).

$$r = \hat{A}k_0\left(1 - \frac{Q_i}{K_{eq}}\right) \qquad \text{Eqn. } 4-9$$

$$k_0 = k_0^* \exp\left[-\frac{E_a}{R}\left(\frac{1}{T} - \frac{1}{T^*}\right)\right] \qquad \text{Eqn. } 4-10$$

$$RSA = SSA * \emptyset_m * M_w * V_m^{-1} \qquad \text{Eqn. } 4-11$$

Where r is the reaction rate, $\hat{A}$ is the reactive surface area, k_0 is the reaction constant, Q is the ion activity product, K_{eq} is the chemical equilibrium constant, E_a is the reaction activation energy, R is the universal gas constant, T is temperature, SSA is the specific surface area, $\emptyset_m$ is mineral volume fraction, M_w is molar weight and V_m is mineral molar volume.

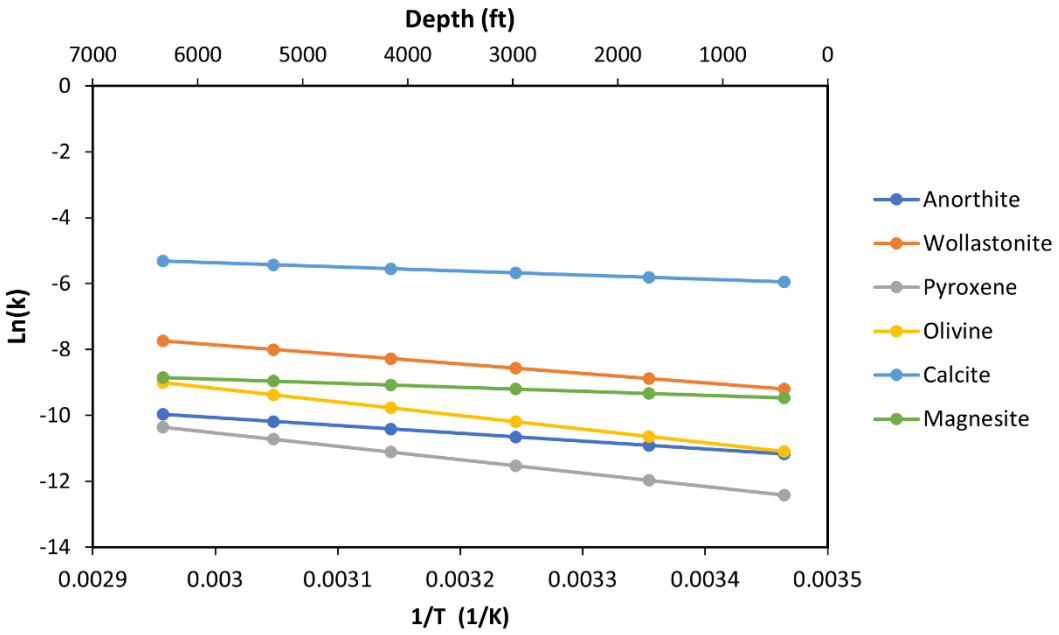

Figure 4-3. Rate Constant changes with depth due to the temperature increases. Higher temperature increases the rate constant and consequently the reaction rate.

Table 4-2. Chemical reactions inputs

Mineral	Formula	Density (g/cm^3)	SSA (m2/g)	RSA (m2/m3)	Log K0	Activation E J/mol
Anorthite	$CaAl_2Si_2O_8$	2.73	3.7	2020200	-10.9	45200
Wollastonite	$CaSiO_3$	2.84	0.8512	24174.08	-8.8	54700
Pyroxene	$MgSiO_3$	3.2	3.7	1657600	-11.9	78000
Olivine	Mg_2SiO_4	3.27	3.7	1693860	-10.6	79000
Calcite	$CaCO_3$			88	-5.81	23500
Magnesite	$MgCO_3$			88	-9.34	23500

The distribution and rate of mineral trapping across the pore space depends on the reaction rate and the dispersion rate of dissolved CO_2. Damköhler number (D_a) is used to relate the reaction rate of reservoir mineral dissolution to the diffusion rate of dissolved CO_2 in water as follows:

$$\mathrm{D_a} = \frac{\text{Reaction Rate}}{\text{diffusion rate}} \qquad \text{Eqn. } 4-12$$

Where the diffusion rate is related to the mass transfer of CO_2 inside the reservoir. McGrail et al. (2006) expressed D_a in the porous media of basaltic formation as follows:

$$\mathrm{D_a} = \frac{\mathrm{S_r f_{Ca} r_d}}{\frac{\beta\,(\rho_s - \rho_o) g\,\mathrm{K}}{\mathrm{v\,L}}\,\mathrm{C_s}} \qquad Eqn. 4-13$$

Where S_r is the specific surface area of the basalt, f_{Ca} is the calcium fraction in basalt, r_d is the normalized release rate of calcium from basalt, β is a porous medium specific coefficient, ρ_s is the desity of CO_2 saturated fluid, ρ_o is the initial fluid density, K is permeability, v is the fluid viscosity, L is the basalt thickness and C_s is the calcium concentration at equilibrium.

In the designed model, the assumption is D_a is bigger than 1 in which the rater of mineralization is limited by the diffusion of CO_2 in the pore space.

4.2. Sensitivity Cases

11 sensitivity cases designed to test the advantage of CO_2 mineral trapping as compared to other trapping mechanisms and to test the parameters that effect CO_2 mineralization.

1. Base Case (Salinity = 80000 ppm, T=123 F, pH= 7)
2. Case 1: No mineral trapping
3. Case 2: No solubility or mineral trapping
4. Case 3: Increase salinity to 120000 ppm
5. Case 4: Increase salinity to 160000 ppm
6. Case 5: Increase salinity to 200000 ppm
7. Case 6: Decrease Salinity to 40000 ppm
8. Case 7: Increase temperature to 130 F
9. Case 8: Increase temperature to 140 F
10. Case 9: Decrease temperature to 110 F
11. Case 10: pH = 9
12. Case 11: pH = 5

Chapter 5 - Numerical simulation and discussion of CO_2 Mineralization in mafic basaltic formations

5.1. Base Model Results

Over 4 years of injection, a total of 16686 tons of CO_2 are injected into the reservoir. The pressure in the reservoir increases during the injection process to 3140 psi which is below the maximum allowable pressure, Figure 5-1. The pressure decreases directly and quickly after the injection stops due to the rapid CO_2 mineralization. Mineralized CO_2 occupies a lower pore space than supercritical and aqueous CO_2. In addition, supercritical and aqueous CO_2 has a higher entropy than solid CO_2 at the same pressure; thus, the mineralization of CO_2 provides a significant advantage of pressure reduction in the reservoir which lowers the possibility of fracturing and leakage. The process of CO_2 mineralization starts within the first year of injection. Figure 5-2 shows that most injected CO_2 is mineralized before the end of injection. The mineralization rate of CO_2 peaked in the first seven years, then slowed down for the next 197 years. The continuation of slow CO_2 mineralization after seven years results in a further decline

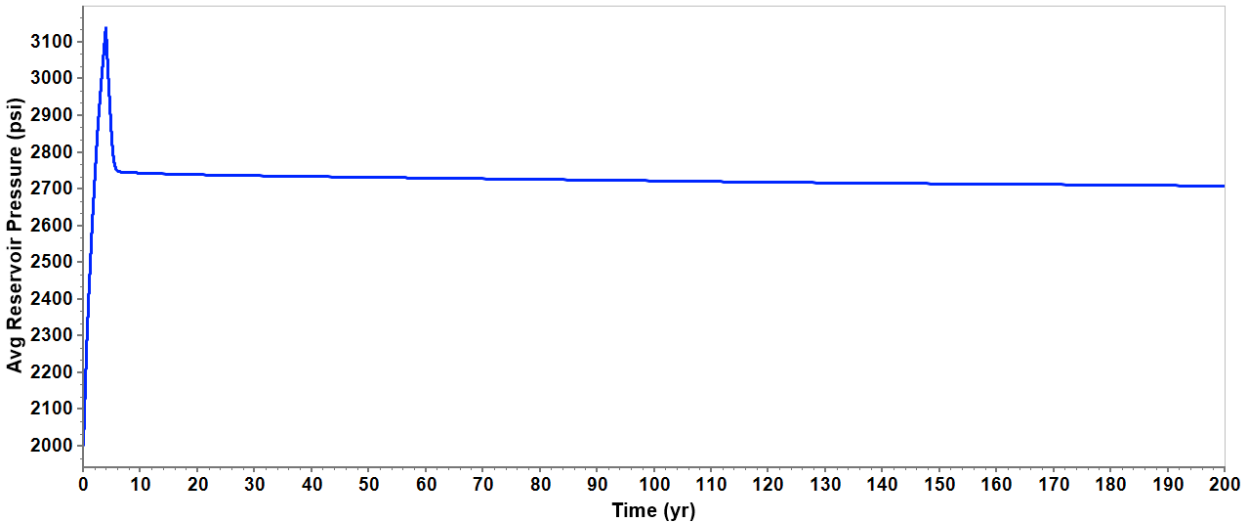

Figure 5-1. Average reservoir pressure declines significantly after injection shut-in due to the continuous CO2 mineralization.

in average reservoir pressure. After 200 years, the average reservoir pressure declines to 2700 psi.

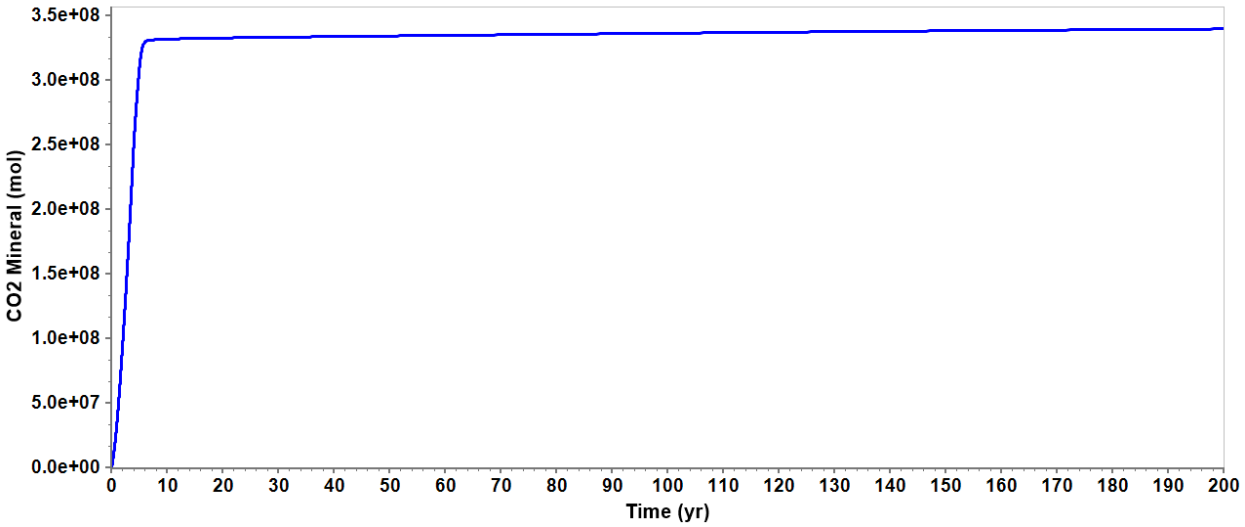

Figure 5-2. 95% of injected CO2 mineralized within the first 7 years. CO2 mineralization continues after 7 years but at very low rate.

CO_2 mineralization indicates that a mineral dissolution of basalt and wollastonite minerals occurred after CO_2 injection. CO_2 mineralizes in the form of calcite and magnesite, which requires calcium and magnesium ions to be released from the dissolution of basalt and wollastonite minerals to bond with carbonate ions from CO_2 dissolution in brine. It is observed that the dissolution of wollastonite and forsterite is the main reason for CO_2 mineralization. The dissolution of wollastonite releases calcium ions that bond with carbonate and mineralize CO_2 in the form of calcite. The dissolution of forsterite releases magnesium ions that bond with carbonate ions and mineralize CO_2 as magnesite. On the other hand, anorthite did not contribute to cations production because it did not dissolve in brine. Likewise, enstatite precipitated after CO_2 injection. The precipitation of enstatite leads to the reduction in magnesium ions available in brine which reduces the amount of CO_2 mineralized in the form of magnesite. Figure 5-3

shows the change in reservoir minerals after CO_2 injection due to dissolution and precipitation. Figure 5-4 shows the precipitation of CO_2 in the form of calcite and magnesite and carbonate minerals. After 200 years, 98% of injected CO_2 was mineralized in the form of carbonate minerals, 10% calcite and 90% magnesite. 0.5% of injected CO_2 is residually trapped and 1.5% is trapped as dissolved in brine.

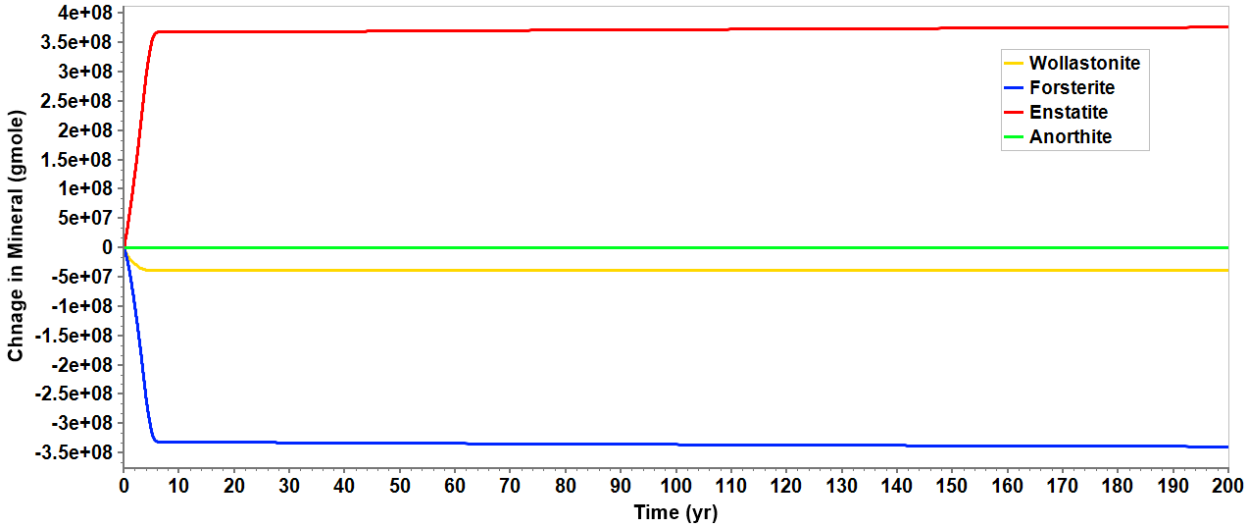

Figure 5-3. The dissolution of forsterite and wollastonite are the source of magnesium and calcium to mineralize CO2 into calcite and magnesite. Enstatite has a negative effect of CO2 mineralization because its precipitation consumes magnesium ions.

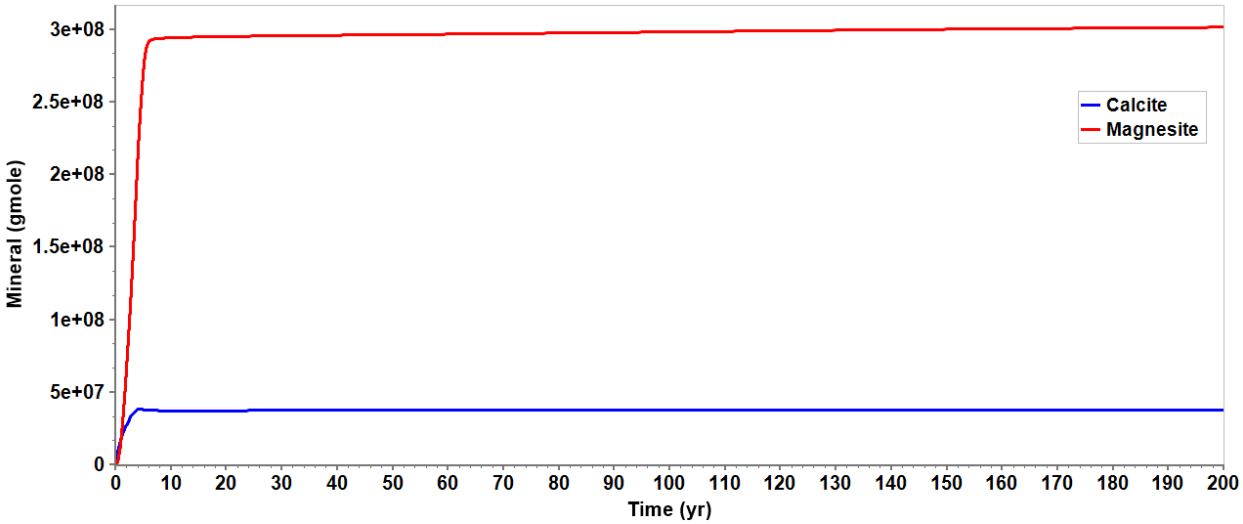

Figure 5-4. CO2 mineralized into calcite (10%) and magnesite (90%). Magnesite continues to precipitate for 200 years due to the continuous dissolution of forsterite.

As illustrated in Figure 5-4 above, calcite stops precipitating completely after 7 years while magnesite continues to precipitate but at a very low rate. Magnesite precipitation continues for 200 years because forsterite is still undergoing dissolution which produces magnesium ions. In addition, as shown in Figure 5-5, there is undissolved supercritical CO_2 that is dissolving in water which produces carbonate ions to bond with magnesium and precipitate into magnesite.

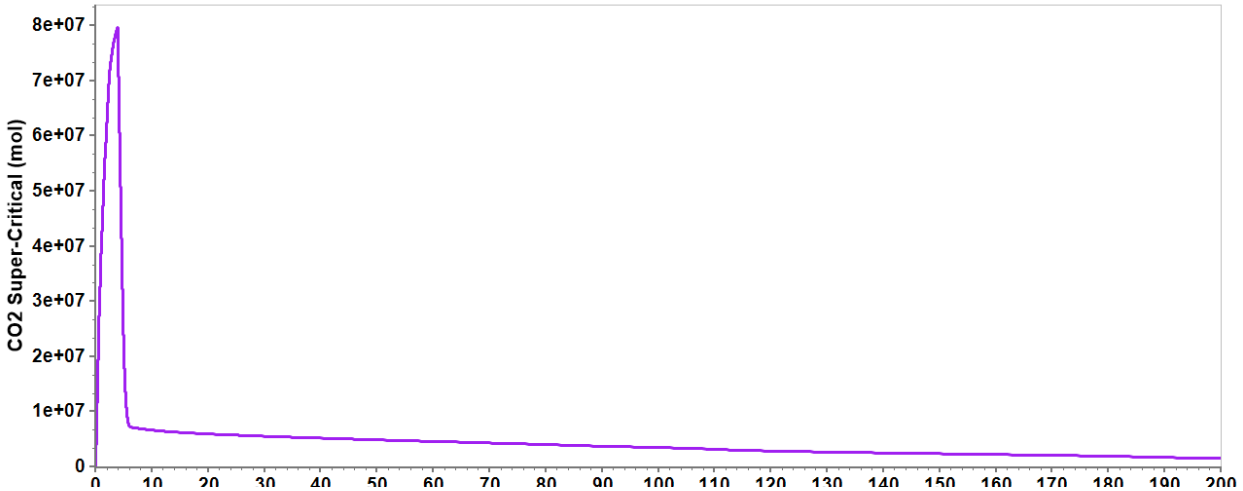

Figure 5-5. The amount of supercritical CO2 declined rapidly after injection shut-in due to dissolution in brine. The dissolution of CO2 in brine continuous for 200 years which results in releasing carbonate ions to bond with calcium and magnesium.

Supercritical CO_2 has a lower density than brine, thus, it will migrate upward due to gravity segregation if not residually trapped or dissolved in brine. Due to the rapid CO_2 dissolution in brine and mineralization, the plume did not migrate far away from the injection well. Figure 5-7 shows CO_2 plumes at different years. Over time as the plume migrates away from the well, most of the CO_2 is dissolved in water and gas saturation is reduced rapidly. Maximum CO_2 saturation and plume migration distance occur at the end of the injection. After four years of injection, CO_2 saturation near the wellbore is 75% maximum and the plume migrated a maximum of 105 ft horizontally and 110 ft above the upper perforation, as illustrated in Figure 5-6.

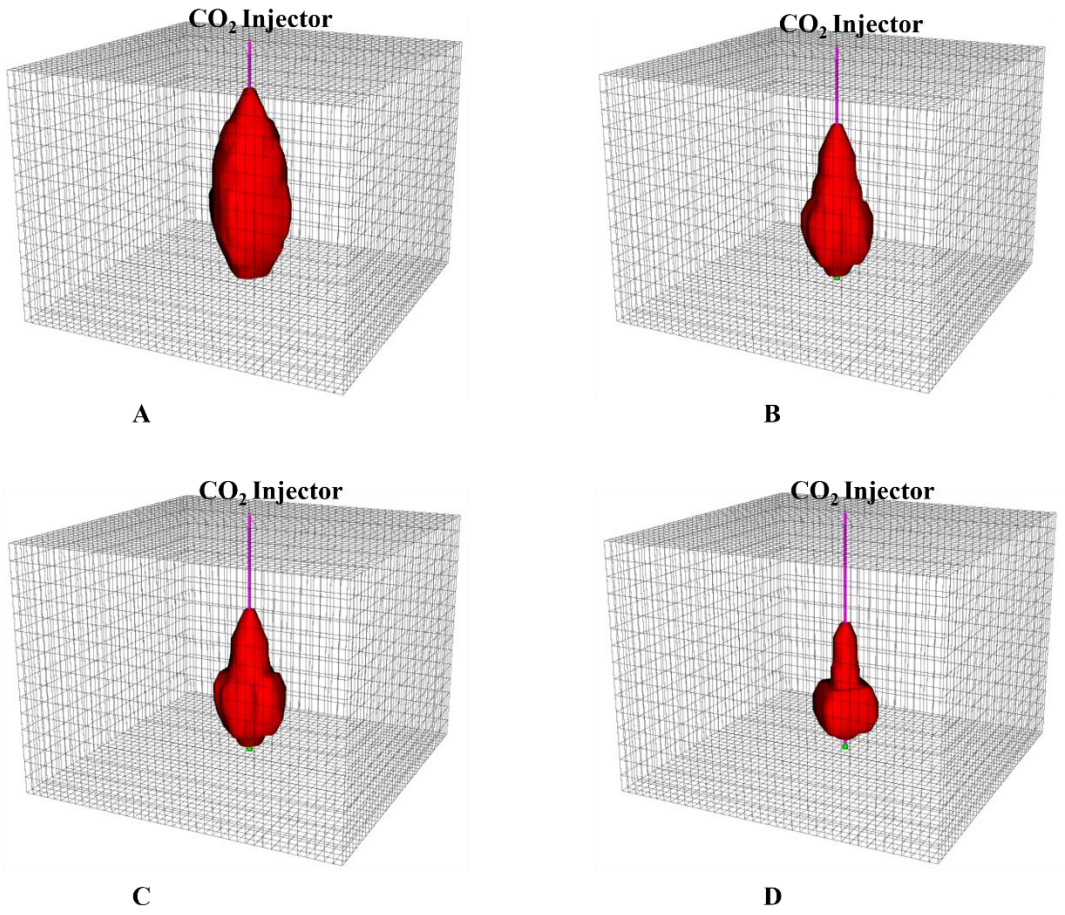

Figure 5-7. CO_2 plume migration after (A) 4 years, (B) 25 years, (C)100 years and (D) 200 years. CO_2 plume declines due to dissolution in brine.

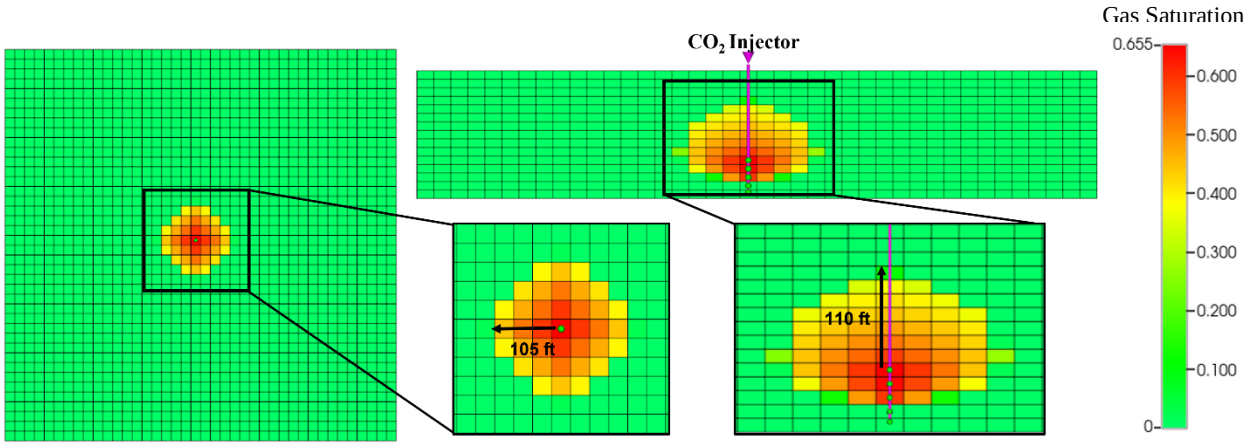

Figure 5-6. Maximum CO_2 saturation is 65.5% which is observed near wellbore at the end of injection. The plume migrated a maximum of 105 ft horizontally and 110 ft vertically from the upper perforation.

The dissolution of CO_2 in brine lowers the pH due to the increase of hydrogen ions in brine. Lowering the pH of brine triggers the chemical reactions toward a new chemical equilibrium inside the reservoir pore space. To reach a new chemical equilibrium, the pH must be increased through the consumption of hydrogen ions by reacting with the reactive minerals in the formation which leads to CO_2 mineralization eventually.

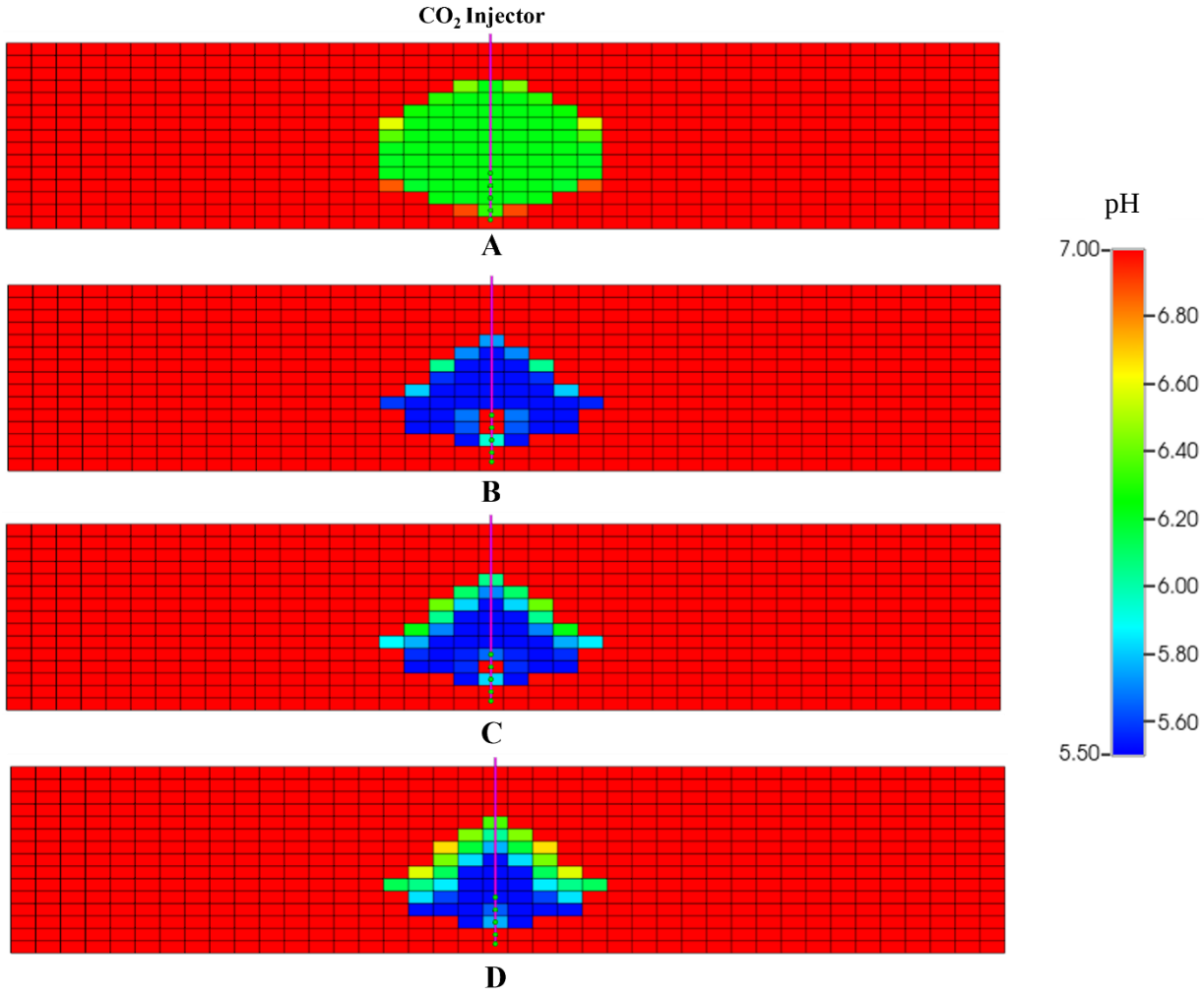

Figure 5-8. The dissolution of CO_2 in brine releases hydrogen ions that lower the pH in the brine. This pH is increased as CO_2 mineralizes into carbonate minerals. Brine pH after (A) 4 years, (B) 25 years, (C)100 years and (D) 200 years.

As shown in Figure 5-8, the initial brine pH is 7 and decreases over time due to the dissolution of CO_2. Near the wellbore areas are the most affected by the reduction in pH. The pH increases in the pore space where mineralization occurs. However, near the wellbore, the mineralization rate is lower than the rate of CO_2 dissolution in brine; thus, the pH continues to decline even with CO_2 mineralization. The lowest brine pH observed near the wellbore is 5.5.

The dissolution of reservoir minerals and precipitation of carbonate minerals results in changing the porosity and permeability. Porosity around the injection well wellbore was reduced by 5% maximum as shown in Figure 5-9. This indicates that the amount of cement in the pore space created by minerals precipitated is more than the cement removed by mineral dissolution. The change in porosity leads to change in permeability. Due to the simulation software limitation, the change in permeability cannot be visualized as with the porosity. However, the change in permeability is reflected by a resistance factor that is calculated using Kozeny-Carman type formula as follows:

$$\mathrm{rf} = \left(\frac{\emptyset_n}{\emptyset_k}\right)^3 \left(\frac{1-\emptyset_k}{1-\emptyset_n}\right)^2 \qquad \text{Eqn. } 5-1$$

Where $\emptyset_n$ and $\emptyset_k$ are previous and current porosity, respectively. Thus, the change in permeability as a function of the resistance factor is expressed as follows:

$$k_k = \frac{k_n}{\mathrm{rf}} \qquad \text{Eqn. } 5-2$$

Where k_n and k_k are previous and current permeability, respectively. As shown in Figure 5-10. The resistance factor increases over time due to the mineralization of CO_2 in pore space. The maximum resistance factor observed is 3.5, meaning permeability decreased to 28.5 md near the wellbore.

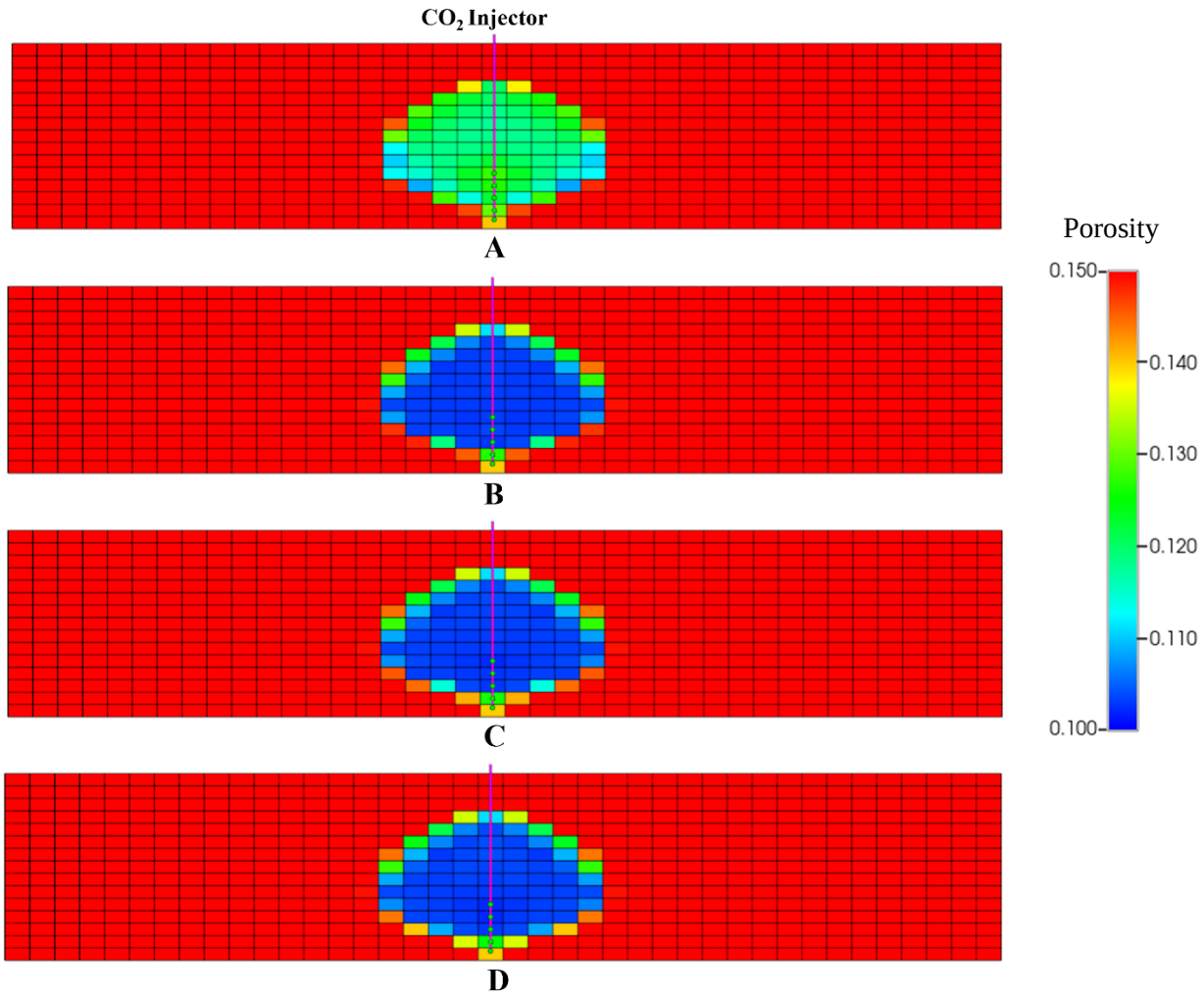

Figure 5-9. Porosity reduces due to the additional cement in the pore space due to CO_2 mineralization. porosity reduced by 5% near wellbore. Porosity changes after (A) 4 years, (B) 25 years, (C)100 years and (D) 200 years.

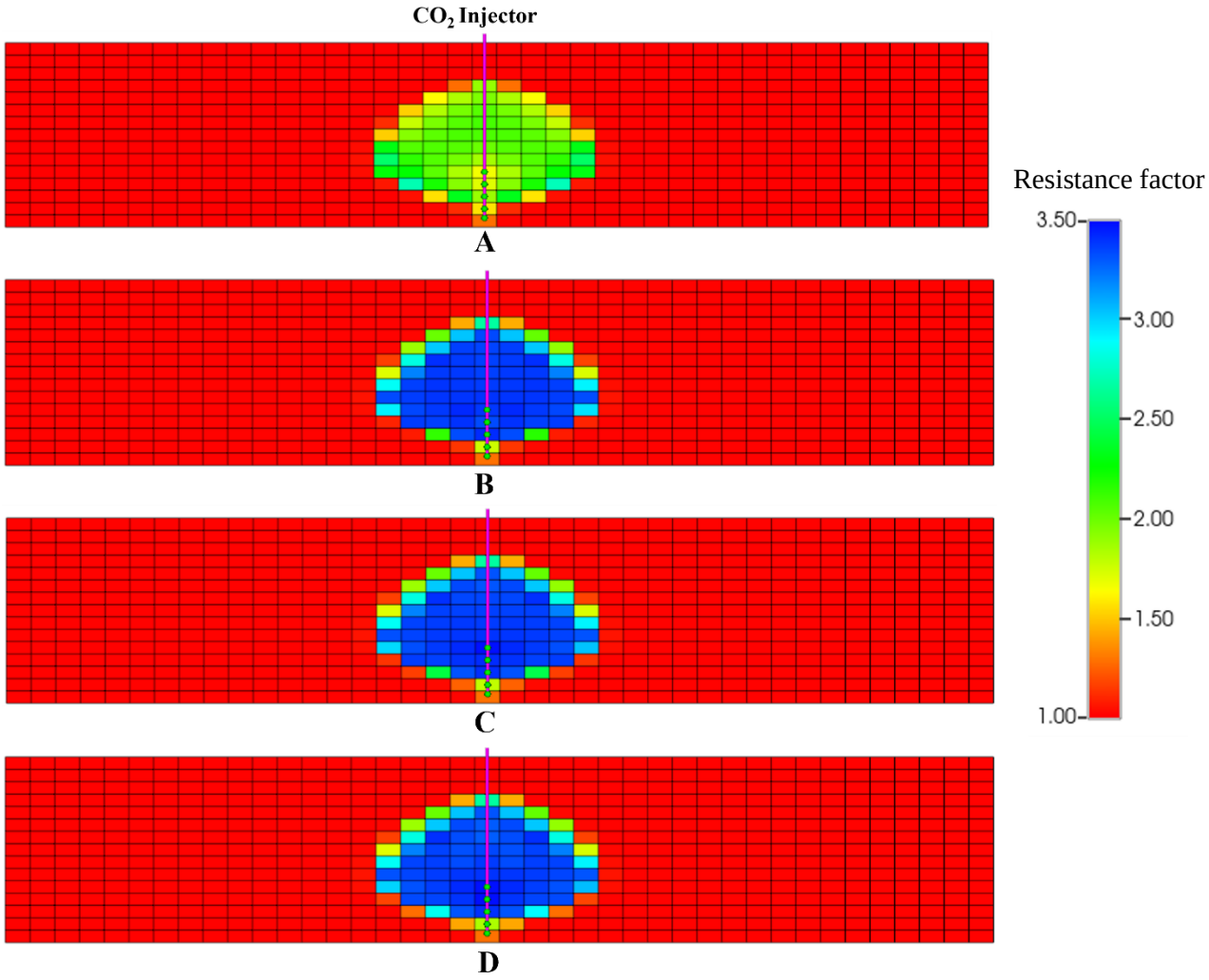

Figure 5-10. The change in permeability is expressed as a resistance factor. The maximum resistance factor is obtained near wellbore which is 3.5 resulting in reducing the permeability from 100 md to 28.5 md. Resistance factor over time at after 4 years, (B) 25 years, (C)100 years and (D) 200 years.

5.2. Sensitivity Analysis

The dynamics in the reservoir pore space after CO_2 injection depends on the initial conditions of the reservoir, including temperature, pressure, brine salinity, and brine pH available. The goal of this sensitivity analysis is to understand how these parameters control the amount of CO_2 dissolution in the brine, mineral dissolution, and mineral precipitation. In addition, the sensitivity analysis will discuss the average reservoir pressure under the assumption

that there is no mineral trapping to understand the effect of CO_2 mineralization on plume migration and average reservoir pressure.

A. CO_2 *mineralization effect on pressure and plume migration*

The main advantage of targeting mafic basaltic formations to store CO_2 is their high reactivity with dissolved CO_2, leading to CO_2 mineralization. As discussed previously, the average reservoir of reservoir declines with CO_2 mineralization because the CO_2 solid phase occupies smaller space and chemical molecules are more stable. In Case 1, mineral trapping is neglected while in Case 2, both mineral trapping and solubility trapping are neglected. Thus, in Case 1, CO_2 will be stored as supercritical fluid or dissolved in brine and in Case 2, CO_2 is stored as supercritical fluid only.

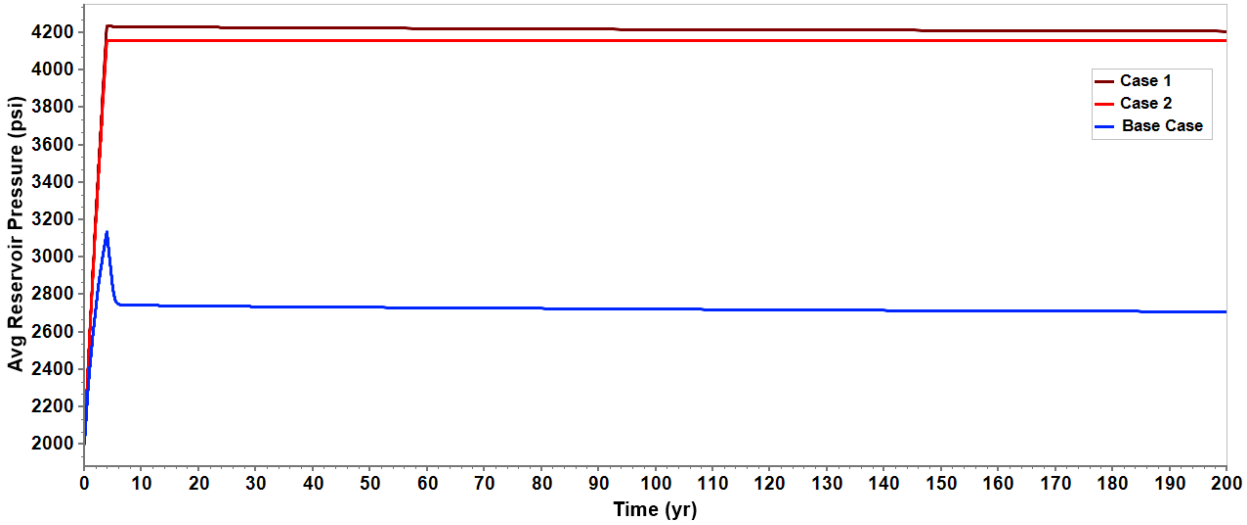

Figure 5-11. Average reservoir pressure is significantly lower when CO_2 mineralization is considered.

As shown in Figure 5-11, the average reservoir pressure at the end of the injection period in Case 1 is 4250 psi, and in Case 2 is 4150 psi. Thus, the average reservoir pressure is around 31% higher than the base case where CO_2 mineralization is considered. Also, the pressure

declines slightly in Case 1 after injection shut-in because of continuous CO_2 dissolution in the brine. However, the pressure declines from injection shut-in to 200 years in Case 1 only by 0.7% while in the Base Case by 15%. In Case 2, there is no pressure decline because CO_2 is not undergoing any phase change.

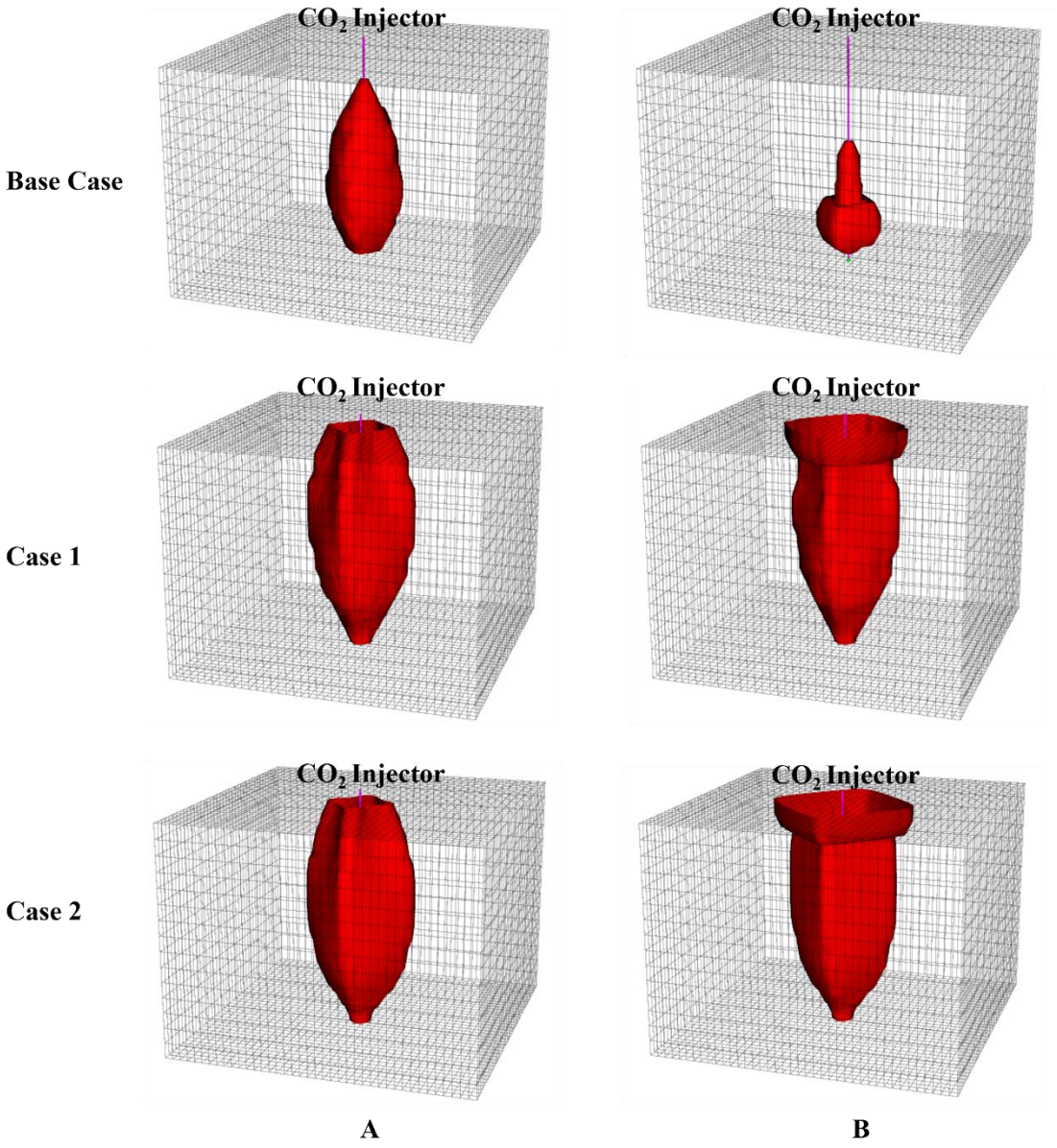

Figure 5-12. CO_2 plume reaches the top layer at the end of the simulation for Case 1 and 2 unlike Base Case where mineralization is simulated. Thus, stored CO_2 in basalt formations has a very low risk of leakage to the surface. A) CO_2 plume at the end of injection, B) CO_2 plume after 200 years.

In addition, CO_2 mineralization reduces the risk of CO_2 leakage to the surface of near surface zones. Supercritical CO_2 has lower density than brine, thus, it will migrate upward to the surface if not residually or structurally trapped. As shown in Figure 5-12, CO_2 plume at the end of injection and after 200 years of simulation did not reach the top layer in the Base Case while it is the contrary for the other two cases. In Case 1 and Case 2, the plume accumulated under the top layer after 200 years.

B. Brine Salinity

CO_2 solubility in brine decreases with increasing salinity, which reduces the amount of hydrogen ions and carbonate ions in brine that is necessary for CO_2 mineralization. As shown in Figure 5-13, the amount of CO_2 dissolved in brine is higher at lower brine salinity.

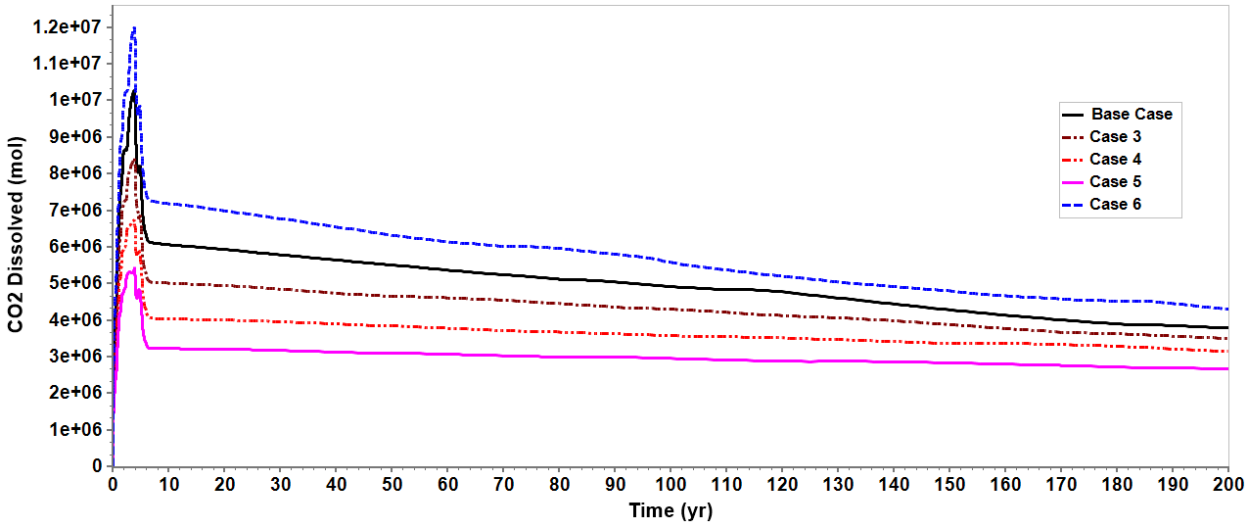

Figure 5-13. CO_2 dissolution in brine is higher at lower salinities.

Also, the amount of CO_2 dissolved in brine continues to decline in lower salinities which indicates CO_2 mineralization. However, the amount of CO_2 mineralized after 200 years is almost the same for all different salinities as shown in Figure 5-14.

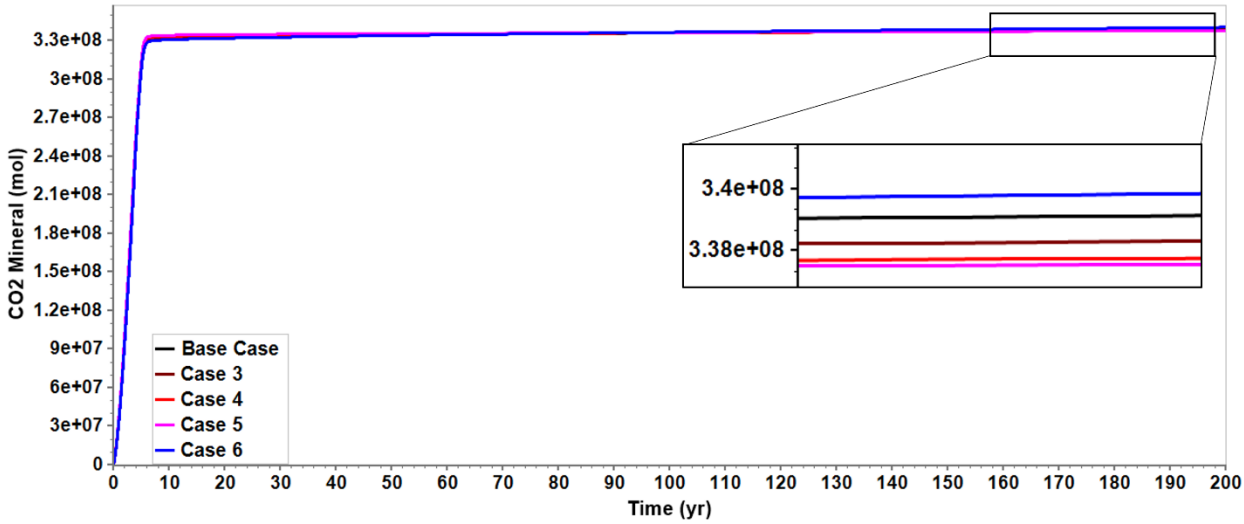

Figure 5-14. CO_2 mineralization at different brine salinity. There is a slight effect on the amount of CO_2 mineralized as salinity changes.

Forming carbonate minerals requires carbonate ions released from water dissolution and cations released from minerals dissolution. Thus, even though lower salinity brine dissolves more CO_2, the formation has the same amount of cations in all cases. The amount of hydrogen ions released in all cases were sufficient to cause the same amount of mineral dissolution. As shown in Figure 5-15, the amount of magnesium ions in brine is stabilized after seven years where CO_2 mineralization stabilizes. Therefore, CO_2 mineralization is affected more by the available cations than brine salinity.

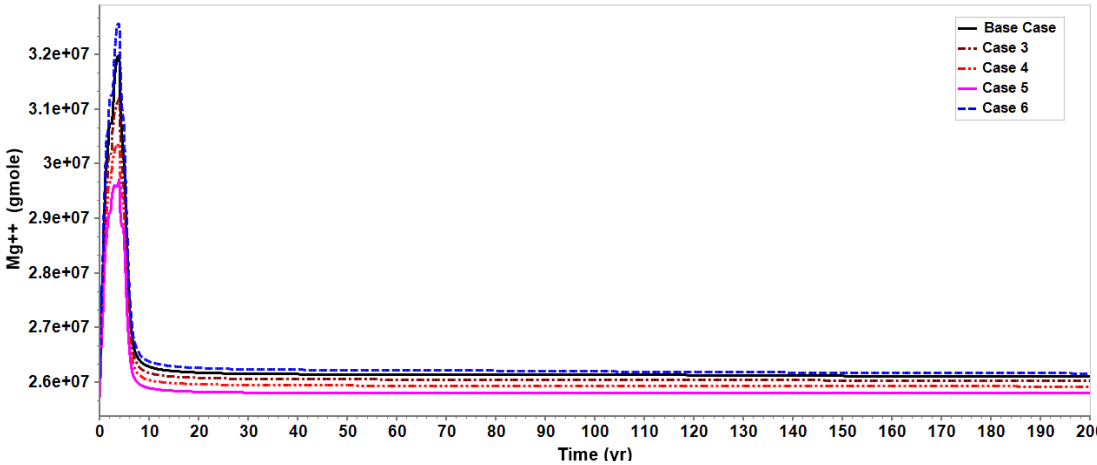

Figure 5-15. Magnesium concentration in brine stabilizes after 7 years at different salinities.

C. Temperature

The temperature has two effects on CO_2 mineralization. First, as the temperature increases, CO_2 solubility in brine decreases, which reduces hydrogen and carbonate ions concentration in brine. On the other hand, higher temperatures increase the mineral dissolution rate, increasing the available cations in brine. As shown in Figure 5-16, mineralized CO_2 is much more elevated at lower temperatures. However, the mineralization rate in the first few years is higher at high temperatures. As shown in Figure 5-17, in the first 4 years, the amount of forsterite dissolved in brine is higher at higher temperatures meaning there are more magnesium ions in brine to bond with carbonate and mineralize into magnesite. In addition, carbonate and hydrogen ions concentrations are lower and are consumed faster in the early time at higher temperatures. Thus, after 8 years, mineralized CO_2 is higher at lower temperatures because of higher CO_2 dissolution in brine.

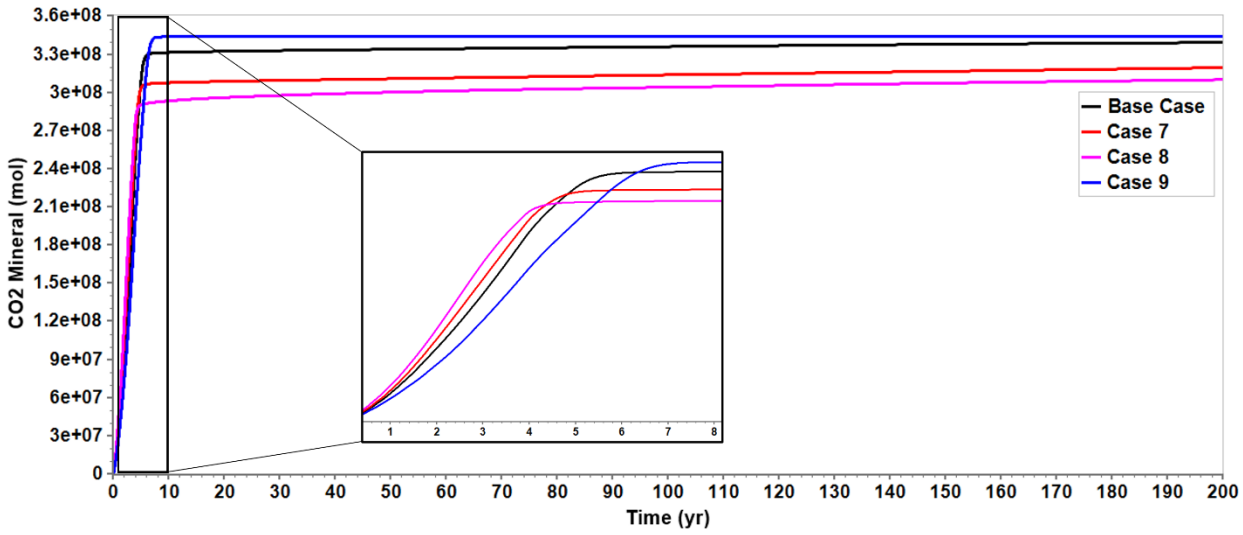

Figure 5-16. CO_2 mineralization at different temperatures. CO_2 is mineralized at higher volumes in lower temperatures.

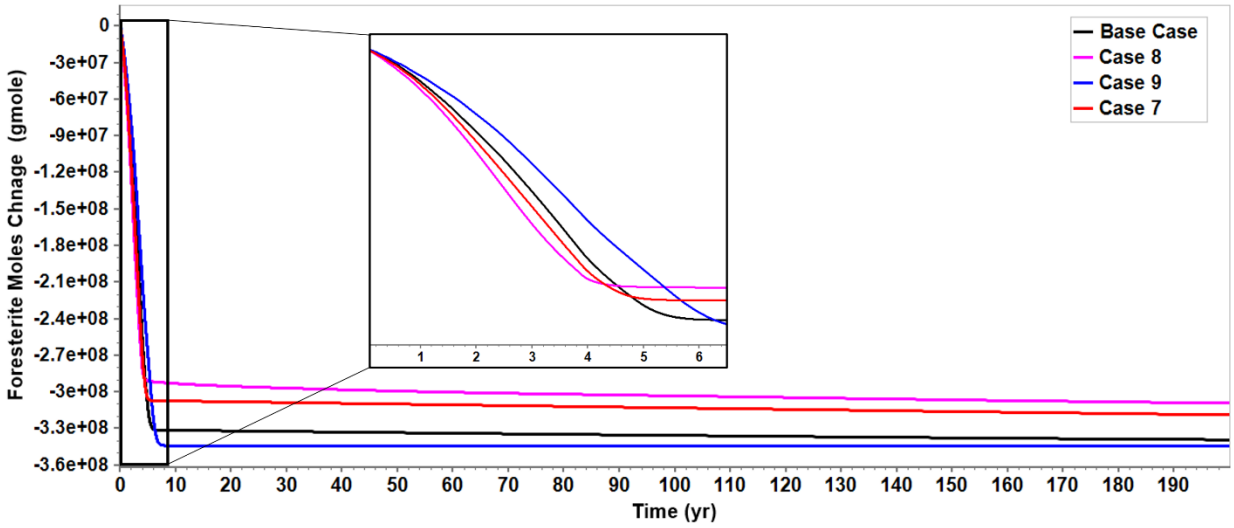

Figure 5-17. Forsterite dissolves faster in brine at higher temperatures.

D. pH

The initial pH of brine indicates the initial concentration of hydrogen ions in brine. The lower the pH, the reservoir mineral dissolution is faster. To release cations from reservoir minerals, hydrogen ions attack the reservoir minerals. Therefore, the lower pH brine has more hydrogen ions to release cations from reservoir minerals. However, over time, As injected CO_2 dissolves in brine, the higher pH brine will initially have a sufficient hydrogen concentration to mineralize the same amount of CO_2. Thus, the initial pH of a brine affects the rate of mineralization, but not the amount of mineralization. as shown in Figure 5-18, lower pH reservoir mineral trapping is completed within the first 10 years, while the higher pH reservoir mineral trapping takes 200 years to mineralize the same amount. Figure 5-19 shows that CO_2 continues to dissolve in the highest pH case for 200 years, indicating a slower CO_2 mineralization.

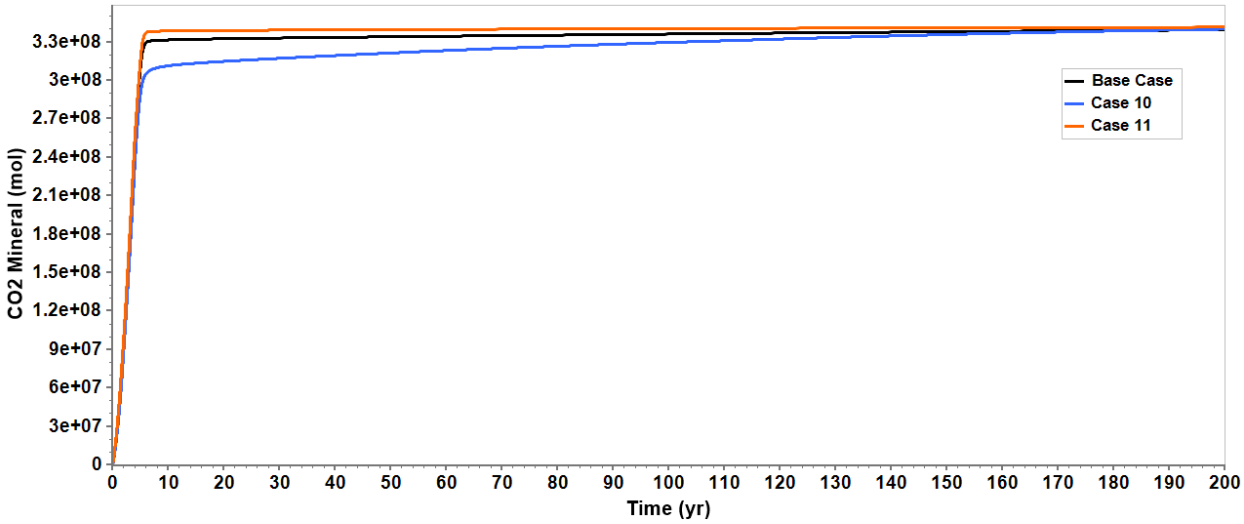

Figure 5-18. CO_2 mineralizes at a faster rate in lower pH brine.

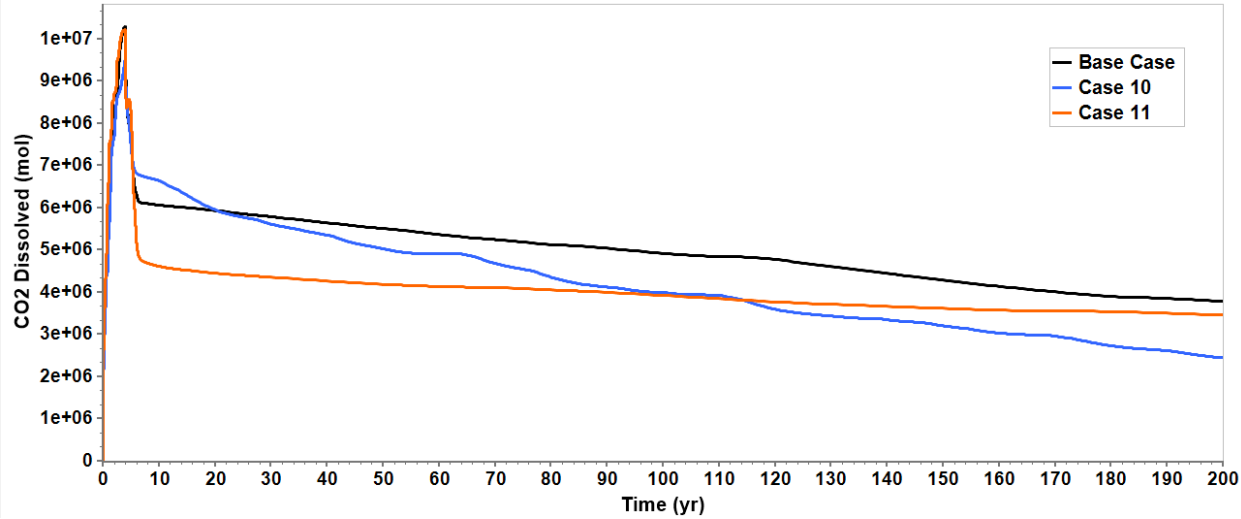

Figure 5-19.Dissolved CO_2 in Case 10 declines throughout the 200 years which indicate a slow rate of mineralization.

Chapter 6 - Conclusions and future work

6.1. Conclusions

CO_2 storage in geological formations is critical to achieving the global goal of net zero by 2050. However, storing CO_2 in geological formations has the risk of leakage to the surface. To minimize this risk, studies have been conducted to store CO_2 in the aqueous phase in brine or mineralized as a carbonate mineral. This research investigates CO2 solubility in brine and storage through mineralization in mafic basaltic formations. Understanding the solubility of CO_2 in brine is critical for CO_2 mineralization. The dissolution of CO_2 in brine after injection triggers the reservoir's geochemical reactions to mineralize CO_2. Basalt formations have an advantage over sedimentary formations as a target for CO_2 mineralization because of their reactive mineral content. This research used a 3D simulation model to simulate the geochemical reaction in a basaltic formation after CO_2 injection. The formation rock is assumed to have 20% plagioclase, 14% olivine, 14% pyroxene, and 1% wollastonite. The main conclusions of the research are:

- The dissolution of CO_2 in brine is controlled by temperature, pressure, and salinity where it increases with pressure and decreases with salinity.
- CO_2 dissolution in brine and mineralization starts within the first year of injection. Most CO_2 is mineralized during the injection period.
- Due to the continuous mineralization of CO_2 after injection shut-in, the average reservoir pressure declines by 15% after injection shut-in.
- 95% of injected CO_2 mineralized within the first 7 years. CO_2 mineralization continues afterward but at a very low rate.
- The amount of CO_2 mineralization into calcite and magnesite depends on the cations released from the formation minerals. Some formation minerals, such as pyroxene,

negatively affected the mount of mineralized CO_2 because pyroxene precipitated after CO_2 injection which consumes magnesium cations from the brine solution that are available to bond with carbonate ions and mineralize into magnesite.

- CO_2 mineralized into calcite (10%) and magnesite (90%). Magnesite continues to precipitate for 200 years due to the continuous dissolution of olivine.
- As CO_2 mineralizes, the concentration of carbonate and hydrogen ions decreases in the brine solution; thus, CO_2 dissolution in brine increases with mineralization and vice versa.
- CO_2 plume does not migrate away from the wellbore due to the rapid mineralization; thus, there is a low risk of leakage to the surface.
- The mineralization of CO_2 reduces porosity by 5% and permeability by 71%. The reduction of porosity and permeability can lead to injectivity issues.
- The maximum permeability and porosity reduction occurs near wellbore which might lead to requiring multiple injection wells to inject large amount of CO_2.
- The average reservoir pressure at the end of injection at a reservoir with no mineralization is 30% higher than a reservoir with mineral trapping.
- In cases with no mineral trapping, the CO_2 plume migrates upward and accumulates under the top layer, the seal, which poses a huge risk of leakage.
- A limited amount of cations can be released from the reactive minerals; thus, in the cases of lower salinity, even though brine dissolution is higher, CO_2 mineralization is almost equal for all cases. This is because in all cases of different salinities, there was enough dissolved CO_2 in brine solution to release the maximum amount of cations.

- Temperature has two effects in CO_2 mineralization. brine dissolution is higher at low temperatures, but the mineral dissolution rate is lower at low temperatures. Overall, CO_2 mineralization is higher at lower temperatures.
- The initial pH of the brine in the reservoir has no effect on the amount of CO_2 mineralized but affects the mineralization rate. The high pH reservoirs mineralize CO_2 at a slower rate.

6.2. Future work

The current model can be improved to simulate CO_2 mineralization and produce additional results to understand the dynamics of geochemical reactions in the deep saline aquifers as follows:

- Considering water vaporization during the simulation to understand the dynamics of CO_2 displacing brine near wellbore and salt-out effect.
- Using an open boundary system will reflect the change in reservoir pressure more accurately than a close boundary system because deep saline aquifers have a very large areal extent.
- Since there is a huge reduction in permeability and porosity due to CO_2 mineralization, using horizontal wells to inject CO_2 might improve CO_2 injectivity.
- Economic evaluation of CO_2 storge in basalt formation. The cost of storing CO_2 in basalt might be higher than in sedimentary formation. Injection CO_2 into basalt requires multiple injection wells due to the quick mineralization around the wellbore that effects CO_2 injectivity.

- Introducing water production wells to the system withdraws water and increases the CO_2 storage capacity.
- Running additional sensitivity analysis cases to understand the effect of reactive surface area and activation energy on CO_2 mineralization.
- Testing different basalt mineralogies.

References

Adams, E Eric and Caldeira, Ken. 2008. Ocean storage of CO2. *Elements* **4** (5): 319-324.

Agartan, Elif, Gaddipati, Manohar, Yip, Yeung et al. 2018. CO2 storage in depleted oil and gas fields in the Gulf of Mexico. *International Journal of Greenhouse Gas Control* **72**: 38-48.

André, Laurent, Audigane, Pascal, Azaroual, Mohamed et al. 2007. Numerical modeling of fluid–rock chemical interactions at the supercritical CO2–liquid interface during CO2 injection into a carbonate reservoir, the Dogger aquifer (Paris Basin, France). *Energy conversion and management* **48** (6): 1782-1797.

Bachu, S and Dusseault, MB. 2005. Underground injection of carbon dioxide in salt beds. *Developments in Water Science* **52**: 637-648.

Bachu, Stefan. 2008. CO2 storage in geological media: Role, means, status and barriers to deployment. *Progress in energy and combustion science* **34** (2): 254-273.

Bakker, Ronald J. 2003. Package FLUIDS 1. Computer programs for analysis of fluid inclusion data and for modelling bulk fluid properties. *Chemical Geology* **194** (1-3): 3-23.

Beckingham, Lauren E, Mitnick, Elizabeth H, Steefel, Carl I et al. 2016. Evaluation of mineral reactive surface area estimates for prediction of reactivity of a multi-mineral sediment. *Geochimica et Cosmochimica Acta* **188**: 310-329.

Birkholzer, Jens T, Oldenburg, Curtis M, and Zhou, Quanlin. 2015. CO2 migration and pressure evolution in deep saline aquifers. *International Journal of Greenhouse Gas Control* **40**: 203-220.

Caldeira, Ken, Akai, Makoto, Brewer, Peter G et al. 2005. Ocean storage.

Celia, Michael Anthony, Bachu, Stefan, Nordbotten, Jan Martin et al. 2015. Status of CO2 storage in deep saline aquifers with emphasis on modeling approaches and practical simulations. *Water Resources Research* **51** (9): 6846-6892.

Chang, Yih-Bor, Coats, Brian K, and Nolen, James S. 1996. A compositional model for CO2 floods including CO2 solubility in water. *Proc.*, Permian Basin Oil and Gas Recovery Conference.

Ciullo, PA and Robinson, S. 2002. WOLLASTONITE A Versatile Functional Filler. *Paint & Coatings Industry* **18** (11): 50-53.

Corum, Margo D, Jones, Kevin B, and Warwick, Peter D. 2013. CO2 sequestration potential of unmineable coal—state of knowledge. *Energy Procedia* **37**: 5134-5140.

Cramer, SD. 1982. Solubility of methane, carbon dioxide, and oxygen in brines from 0/sup 0/to 300/sup 0/C, Bureau of Mines, Pittsburgh, PA.

da Costa, Alvaro Maia, Costa, Pedro VM, Miranda, Antonio CO et al. 2019. Experimental salt cavern in offshore ultra-deep water and well design evaluation for CO2 abatement. *International Journal of Mining Science and Technology* **29** (5): 641-656.

Dabirian, Ramin, Beiranvand, M, and Aghahoseini, Sepehr. 2012. Mineral carbonation in peridotite rock for CO2 sequestration and a method of leakage reduction of CO2 in the rock. *Nafta* **63** (1-2): 44-48.

Daval, Damien, Martinez, Isabelle, Corvisier, Jérôme et al. 2009. Carbonation of Ca-bearing silicates, the case of wollastonite: Experimental investigations and kinetic modeling. *Chemical Geology* **265** (1-2): 63-78.

De Silva, GPD, Ranjith, Pathegama G, and Perera, MSA. 2015. Geochemical aspects of CO2 sequestration in deep saline aquifers: A review. *Fuel* **155**: 128-143.

Ding, Wenjin, Fu, Liangjie, Ouyang, Jing et al. 2014. CO2 mineral sequestration by wollastonite carbonation. *Physics and Chemistry of Minerals* **41** (7): 489-496.
Dong, Kangyin, Jiang, Hongdian, Sun, Renjin et al. 2019. Driving forces and mitigation potential of global CO2 emissions from 1980 through 2030: Evidence from countries with different income levels. *Science of the Total Environment* **649**: 335-343.
Duan, Zhenhao and Sun, Rui. 2003. An improved model calculating CO2 solubility in pure water and aqueous NaCl solutions from 273 to 533 K and from 0 to 2000 bar. *Chemical geology* **193** (3-4): 257-271.
Dusseault, MB, Bachu, S, and Rothenburg, L. 2004. Sequestration of CO2 in salt caverns. *Journal of Canadian Petroleum Technology* **43** (11).
Foroozesh, Jalal, Dier, Monychol Adhil, and Rezk, Mohamed Gamal. 2018. A simulation study on CO2 sequestration in saline aquifers: trapping mechanisms and risk of CO2 leakage. *Proc.*, MATEC Web of Conferences03004.
Godec, Michael, Koperna, George, and Gale, John. 2014. CO2-ECBM: a review of its status and global potential. *Energy Procedia* **63**: 5858-5869.
Gorecki, Charles D, Sorensen, James A, Bremer, Jordan M et al. 2009. Development of storage coefficients for determining the effective CO2 storage resource in deep saline formations. *Proc.*, SPE International Conference on CO2 Capture, Storage, and Utilization.
Hangx, Suzanne JT and Spiers, Christopher J. 2009. Reaction of plagioclase feldspars with CO2 under hydrothermal conditions. *Chemical Geology* **265** (1-2): 88-98.
Hannis, Sarah, Lu, Jiemin, Chadwick, Andy et al. 2017. CO2 storage in depleted or depleting oil and gas fields: what can we learn from existing projects? *Energy Procedia* **114**: 5680-5690.
Harvey, Allan H. 1996. Semiempirical correlation for Henry's constants over large temperature ranges. *AIChE journal* **42** (5): 1491-1494.
Hoteit, Hussein, Fahs, Marwan, and Soltanian, Mohamad Reza. 2019. Assessment of CO2 injectivity during sequestration in depleted gas reservoirs. *Geosciences* **9** (5): 199.
House, Kurt Zenz, Schrag, Daniel P, Harvey, Charles F et al. 2006. Permanent carbon dioxide storage in deep-sea sediments. *Proceedings of the National Academy of Sciences* **103** (33): 12291-12295.
Hughes, David S. 2009. Carbon storage in depleted gas fields: Key challenges. *Energy Procedia* **1** (1): 3007-3014.
Ibrahim, Ahmed Farid and Nasr-El-Din, Hisham A. 2015. CO2 Sequestration in Unmineable Coal Seams. *Proc.*, SPE/IATMI Asia Pacific Oil & Gas Conference and Exhibition.
IEA. 2022. *Global Energy Review: CO2 Emissions in 2021-Global Emissions Rebound Sharply to Highest Ever Level*, International Energy Agency Paris, France (Reprint).
IEA, P. 2020. CCUS in clean energy transitions. In *Technical Report*.
Jayasekara, DW, Ranjith, PG, Wanniarachchi, WAM et al. 2020. Effect of salinity on supercritical CO2 permeability of caprock in deep saline aquifers: An experimental study. *Energy* **191**: 116486.
Jiang, Fei and Tsuji, Takeshi. 2014. Changes in pore geometry and relative permeability caused by carbonate precipitation in porous media. *Physical Review E* **90** (5): 053306.
Kashim, M Zuhaili, Tsegab, Haylay, Rahmani, Omeid et al. 2020. Reaction mechanism of wollastonite in situ mineral carbonation for CO2 sequestration: effects of saline conditions, temperature, and pressure. *ACS omega* **5** (45): 28942-28954.

Kieffer, Bruno, Jové, Carlos F, Oelkers, Eric H et al. 1999. An experimental study of the reactive surface area of the Fontainebleau sandstone as a function of porosity, permeability, and fluid flow rate. *Geochimica et Cosmochimica Acta* **63** (21): 3525-3534.

Kumar, Ajitabh, Ozah, R, Noh, M et al. 2005. Reservoir simulation of CO2 storage in deep saline aquifers. *Spe Journal* **10** (03): 336-348.

Land, Carlon S. 1968. Calculation of imbibition relative permeability for two-and three-phase flow from rock properties. *Society of Petroleum Engineers Journal* **8** (02): 149-156.

Le Gallo, Yann, Couillens, Philippe, and Manai, Taoufik. 2002. CO2 sequestration in depleted oil or gas reservoirs. *Proc.*, SPE International Conference on Health, Safety and Environment in Oil and Gas Exploration and Production.

Li, Jun, Ahmed, Raheel, and Li, Xiaochun. 2018. Thermodynamic modeling of CO2-N2-O2-Brine-Carbonates in conditions from surface to high temperature and pressure. *Energies* **11** (10): 2627.

Luhmann, Andrew J, Kong, Xiang-Zhao, Tutolo, Benjamin M et al. 2014. Experimental dissolution of dolomite by CO2-charged brine at 100 C and 150 bar: Evolution of porosity, permeability, and reactive surface area. *Chemical Geology* **380**: 145-160.

Luo, Shu, Xu, Ruina, and Jiang, Peixue. 2012. Effect of reactive surface area of minerals on mineralization trapping of CO 2 in saline aquifers. *Petroleum Science* **9**: 400-407.

Martin-Roberts, Emma, Scott, Vivian, Flude, Stephanie et al. 2021. Carbon capture and storage at the end of a lost decade. *One Earth* **4** (11): 1569-1584.

Mathias, Simon A, Gluyas, Jon G, Oldenburg, Curtis M et al. 2010. Analytical solution for Joule–Thomson cooling during CO2 geo-sequestration in depleted oil and gas reservoirs. *International Journal of Greenhouse Gas Control* **4** (5): 806-810.

McGrail, B Peter, Schaef, H Todd, Ho, Anita M et al. 2006. Potential for carbon dioxide sequestration in flood basalts. *Journal of Geophysical Research: Solid Earth* **111** (B12).

Mitchell, Mark J, Jensen, Oliver E, Cliffe, K Andrew et al. 2010. A model of carbon dioxide dissolution and mineral carbonation kinetics. *Proceedings of the Royal Society A: Mathematical, Physical and Engineering Sciences* **466** (2117): 1265-1290.

Moita, Patrícia, Berrezueta, Edgar, Abdoulghafour, Halidi et al. 2020. Mineral Carbonation of CO2 in Mafic Plutonic Rocks, II—Laboratory Experiments on Early-Phase Supercritical CO2–Brine–Rock Interactions. *Applied Sciences* **10** (15): 5083.

Mukherjee, Manab and Misra, Santanu. 2018. A review of experimental research on Enhanced Coal Bed Methane (ECBM) recovery via CO2 sequestration. *Earth-Science Reviews* **179**: 392-410.

Olajire, Abass A. 2013. A review of mineral carbonation technology in sequestration of CO2. *Journal of Petroleum Science and Engineering* **109**: 364-392.

Oldenburg, Curtis M. 2007. Joule-Thomson cooling due to CO2 injection into natural gas reservoirs. *Energy Conversion and Management* **48** (6): 1808-1815.

Postma, Tom JW, Bandilla, Karl W, and Celia, Michael A. 2022. Implications of CO2 mass transport dynamics for large-scale CCS in basalt formations. *International Journal of Greenhouse Gas Control* **121**: 103779.

Pruess, Karsten and Garcia, Julio. 2002. Multiphase flow dynamics during CO2 disposal into saline aquifers. *Environmental Geology* **42** (2): 282-295.

Raza, Arshad, Glatz, Guenther, Gholami, Raoof et al. 2022. Carbon mineralization and geological storage of CO2 in basalt: Mechanisms and technical challenges. *Earth-Science Reviews* **229**: 104036.

Ridha, S, Pratama, Edo, and Ismail, Mohd. 2017. Performance assessment of CO2 sequestration in a horizontal well for enhanced coalbed methane recovery in deep unmineable coal seams. *Chemical Engineering Transactions* **56**: 589-594.

Ritchie, Hannah, Roser, Max, and Rosado, Pablo. 2020. CO_2 and greenhouse gas emissions. *Our world in data*.

Romanov, Vyacheslav, Soong, Yee, Carney, Casey et al. 2015. Mineralization of carbon dioxide: a literature review. *ChemBioEng Reviews* **2** (4): 231-256.

Sadeghi, Mohammadamin, Salami, Hossein, Taghikhani, Vahid et al. 2015. A comprehensive study on CO2 solubility in brine: Thermodynamic-based and neural network modeling. *Fluid Phase Equilibria* **403**: 153-159.

Saul, A and Wagner, Wolfgang. 1987. International equations for the saturation properties of ordinary water substance. *Journal of Physical and Chemical Reference Data* **16** (4): 893-901.

Schwartz, Michael O. 2022. Modelling a basalt reactor for direct air CO2 capture. *Environmental Earth Sciences* **81** (7): 1-9.

Sheps, KM, Max, MD, Osegovic, JP et al. 2009. A case for deep-ocean CO2 sequestration. *Energy Procedia* **1** (1): 4961-4968.

Shi, JQ and Durucan, S. 2005a. CO2 storage in caverns and mines. *Oil & gas science and technology* **60** (3): 569-571.

Shi, JQ and Durucan, S. 2005b. CO2 storage in deep unminable coal seams. *Oil & gas science and technology* **60** (3): 547-558.

Sminchak, Joel, Gupta, Neeraj, Byrer, Charles et al. 2001. Issues related to seismic activity induced by the injection of CO2 in deep saline aquifers, National Energy Technology Laboratory (NETL), Pittsburgh, PA, Morgantown, WV ….

Snæbjörnsdóttir, Sandra Ó, Sigfússon, Bergur, Marieni, Chiara et al. 2020. Carbon dioxide storage through mineral carbonation. *Nature Reviews Earth & Environment* **1** (2): 90-102.

Spycher, Nicolas, Pruess, Karsten, and Ennis-King, Jonathan. 2003. CO2-H2O mixtures in the geological sequestration of CO2. I. Assessment and calculation of mutual solubilities from 12 to 100 C and up to 600 bar. *Geochimica et cosmochimica acta* **67** (16): 3015-3031.

Steel, Luc, Liu, Qi, Mackay, Eric et al. 2016. CO2 solubility measurements in brine under reservoir conditions: A comparison of experimental and geochemical modeling methods. *Greenhouse Gases: Science and Technology* **6** (2): 197-217.

Su, Erlei, Liang, Yunpei, Zou, Quanle et al. 2019. Analysis of effects of CO2 injection on coalbed permeability: implications for coal seam CO2 sequestration. *Energy & Fuels* **33** (7): 6606-6615.

Toolbox, TE. Minerals-Densities.

Voormeij, Danae A and Simandl, George J. 2002. Geological and mineral CO2 sequestration options: a technical review. *British Columbia Geological Survey, Geological Fieldwork* **265**.

Wang, Zan, Small, Mitchell J, and Karamalidis, Athanasios K. 2013. Multimodel predictive system for carbon dioxide solubility in saline formation waters. *Environmental science & technology* **47** (3): 1407-1415.

Warren, John Keith. 2017. Salt usually seals, but sometimes leaks: Implications for mine and cavern stabilities in the short and long term. *Earth-science reviews* **165**: 302-341.

White, Curt M, Smith, Duane H, Jones, Kenneth L et al. 2005. Sequestration of carbon dioxide in coal with enhanced coalbed methane recovery a review. *Energy & Fuels* **19** (3): 659-724.

White, Curt M, Strazisar, Brian R, Granite, Evan J et al. 2003. Separation and capture of CO2 from large stationary sources and sequestration in geological formations—coalbeds and deep saline aquifers. *Journal of the Air & Waste Management Association* **53** (6): 645-715.

Xiong, Wei, Wells, Rachel K, Horner, Jake A et al. 2018. CO2 mineral sequestration in naturally porous basalt. *Environmental Science & Technology Letters* **5** (3): 142-147.

Yang, Fang, Bai, Baojun, Tang, Dazhen et al. 2010. Characteristics of CO_2 Sequestration in Saline Aquifers.

Zhang, Shuo and DePaolo, Donald J. 2017. Rates of CO2 mineralization in geological carbon storage. *Accounts of chemical research* **50** (9): 2075-2084.

Zhang, Xiong, Liu, Wei, Chen, Jie et al. 2022. Large-scale CO2 disposal/storage in bedded rock salt caverns of China: An evaluation of safety and suitability. *Energy* **249**: 123727.

Ziabakhsh-Ganji, Zaman and Kooi, Henk. 2014. Sensitivity of Joule–Thomson cooling to impure CO2 injection in depleted gas reservoirs. *Applied energy* **113**: 434-451.

Zivar, Davood, Kumar, Sunil, and Foroozesh, Jalal. 2021. Underground hydrogen storage: A comprehensive review. *International journal of hydrogen energy* **46** (45): 23436-23462.